

MAGNETIC ANISOTROPIES AND DYNAMIC MAGNETIC
PROPERTIES IN MULTILAYERED THIN FILMS

by

JAMILEH BEIK MOHAMMADI

TIM MEWES, COMMITTEE CHAIR

CLAUDIA K. A. MEWES

ARUN GUPTA

GARY J. MANKEY

PATRICK R. LECLAIR

DAWN R. WILLIAMS

A DISSERTATION

Submitted in partial fulfillment of the requirements
for the degree of Doctor of Philosophy
in the Department of Physics and Astronomy
in the Graduate School of
The University of Alabama

TUSCALOOSA, ALABAMA

2017

Copyright Jamileh Beik Mohammadi 2017
ALL RIGHTS RESERVED

ABSTRACT

Theoretical and experimental research on magnetic materials and magnetic devices intend to investigate novel materials and structures which can be used for the next generation spintronic devices. Moreover, it is essential to conduct fundamental research on new phenomena aiming for new generation of devices that can be faster, smaller, cheaper, and more reliable.

Magnetic anisotropies have been widely used in spintronic devices. From the unidirectional exchange bias anisotropy that is used in magnetic read heads and giant magnetic resonance (GMR) sensors, to the interfacial perpendicular magnetic anisotropy (PMA) that is essential for magnetic tunnel junctions (MTJs). In the first chapter of this dissertation a short introduction to magnetization dynamics including experimental techniques is given. In the second chapter, the exchange bias anisotropy and the interfacial origin of relaxation in Ru/IrMn/CoFe/Ru exchange biased systems is discussed and investigated. The interfacial perpendicular anisotropy is observed in these systems and can be quantified using FMR technique. Such anisotropy can exist in a thin ferromagnetic film (such as NiFe) that is in proximity to a metallic (e.g. Ru) or insulating (e.g. SiO₂) non-magnetic layer, which is the topic of the third chapter of this dissertation. In addition, experimental results confirm that spatial fluctuations of the uniaxial perpendicular anisotropy can push the easy axis of the magnetization in an orientation that is neither perpendicular to the film nor normal to it. The effect of the lateral

fluctuation of the uniaxial anisotropy on the magnetic energy landscape and the magnetization dynamics of thin magnetic layers is reported in chapter four using micromagnetic simulations.

DEDICATION

To the memory of my parents,

Zafar and Soraya

to my better half Saman Salari,

and to my beloved siblings...

LIST OF ABBREVIATIONS AND SYMBOLS

LLG	Landau-Lifshitz-Gilbert
FM	Ferromagnetic
SI	International System of Units
CGS	Centimeter–Gram–Second system of units
BLS	Brillouin Light Scattering
FMR	Ferromagnetic Resonance
AC	Alternative Current
RF	Radio Frequency
XRR	X-Ray Reflectivity
XRD	X-Ray Diffraction
PMA	Perpendicular Magnetic Anisotropy
AF	Antiferromagnetic
TMS	Two-Magnon-Scattering
MTJ	Magnetic Tunnel Junction
MOKE	Magneto-Optical Kerr Effect
STT-MRAM	Spin Transfer Torque Magnetic Random Access Memory
FFT	Fast Fourier Transform
XMCD	X-Ray Magnetic Circular Dichroism
PNR	Polarized neutron Reflectivity

ACKNOWLEDGEMENTS

My deepest gratitude goes to my advisor Dr. Tim Mewes and my co-advisor Dr. Claudia Mewes who supported me to the fullest during the past six years at The University of Alabama. Without their continuous encouragements, this dissertation could not be completed. I also appreciate the support from NSF-CAREER Award No. 0952929 and NSF-CAREER Award No. 1452670.

My great appreciation goes to my PhD and Masters' and PhD graduate advisory committee, Dr. William Butler, Dr. Arun Gupta, Dr. Dawn Williams, Dr. Gary Mankey, Dr. Patrick LeClair for their valuable inputs during the past years. I especially thank Dr. Christian Kaiser (Western Digital company) for providing samples and his support and collaboration.

My appreciation extends to my friends and collaborators Dr. Michael Buettner, Jon Steen, Dr. Tanya Gille, Dr. Behrouz Khodadadi, Dr. Neha Pauchari, Dr. Nariman Naghibolashrafi, Dr. Archana Panikar, Amit Singh, Joshua Jones, Saeideh Mirghorbani, Niloofer Toorchi, Kayla Cole, Alison Farrar, Abhishek Srivastava, Anish Rai, Arjun Sapkota, Mareike Dunz, Smriti Ranjit, for helping me by all means throughout my PhD years.

I am especially thankful for the technical support provided by physics department machine shop staff and electronic technicians Joe Howell, David Key, Danny Whitcomb and Jason Kuykendall. I particularly want to thank Ms. Michele Kijeski for helping me with all the administrative paper work.

I can not thank my family members enough for being my biggest supporters and constantly putting my success and happiness before their own. Their love is irreplaceable.

CONTENTS

ABSTRACT.....	ii
DEDICATION.....	iv
LIST OF ABBREVIATIONS AND SYMBOLS	v
ACKNOWLEDGEMENTS.....	vi
LIST OF FIGURES	xi
1. INTRODUCTION	1
I. Magnetization dynamics	1
II. Experimental procedure	3
A. Ferromagnetic resonance technique	3
B. Magnetron sputtering.....	6
C. X-Ray reflectivity experiment	7
III. Micromagnetic simulations	9
IV. Magnetic anisotropy and relaxation study	10
2. BROADBAND FERROMAGNETIC RESONANCE CHARACTERIZATION OF ANISOTROPIES AND RELAXATION IN EXCHANGE BIASED IrMn/CoFe BILAYERES [Reformatted reprint of Ref. 26]	13
I. Introduction.....	14

II.	Experimental procedures.....	15
III.	Ferromagnetic resonance in exchange bias system.....	16
IV.	Magnetic anisotropies	19
A.	Broadband FMR characterization.....	19
B.	In-plane angle dependent characterization	21
V.	Magnetization relaxation.....	27
VI.	Summary	33
VII.	Acknowledgements	35
VIII.	References	36
3.	FERROMAGNETIC RESONANCE STUDY OF INTERFACIAL PERPENDICULAR ANISOTROPY IN $\text{Ni}_{0.8}\text{Fe}_{0.2}/\text{Ru}$ AND $\text{Ni}_{0.8}\text{Fe}_{0.2}/\text{SiO}_2$ INTERFACES [Reformatted reprint of Ref. 30]	41
I.	Introduction.....	41
II.	Experimental procedure	42
III.	Results and discussion.....	43
IV.	Conclusion.....	48
V.	Acknowledgements	48
VI.	References.....	49
4.	INHOMOGENEOUS PERPENDICULAR MAGNETIC ANISOTROPY AS A SOURCE OF HIGHER-ORDER QUASI-STATIC AND DYNAMIC ANISOTROPIES [Reformatted reprint of Ref. 31]	52
I.	Introduction.....	53

II.	Results and discussion.....	54
A.	Theoretical background (Methodology).....	54
B.	Quasi-static properties	56
C.	Influence of length scale of lateral anisotropy variations.....	63
D.	Dynamic properties.....	67
III.	Summary and discussion.....	73
IV.	Acknowledgments	74
V.	References	75
5.	CONCLUSION.....	78
6.	REFERENCES	81

LIST OF FIGURES

<p>FIG 1.1. Schematics of the applied quasi-static field H, microwave field h_{mw}, and the magnetization M for a ferromagnetic thin film in the xy plane. In general, the magnetization vector is not aligned with the applied field. ϕ_0 and θ_0 are the azimuthal angle of the magnetization vector (measured from x axis) and the polar angle of the magnetization vector (measured from z axis), respectively. ϕ_H and θ_H represent the azimuthal and polar angle of H, respectively.</p>	2
<p>FIG 1.2. A typical raw FMR data at a fixed frequency. The black line shows the experimental FMR data and the red line is the fit to Eq. (1.5).</p>	3
<p>FIG. 1.3. Broadband ferromagnetic resonance (FMR) setup. The setup is capable of performing polar (θ), and azimuthal (ϕ) angular dependent measurements.</p>	6
<p>FIG. 1.4. A typical XRR data. Intensity (counts) is plotted vs. angle θ in range of 0.01 rad to 0.05 rad. Dashed lines correspond to local intensity maxima where $\theta = \theta_m$.</p>	8
<p>FIG. 1.5. Symbols represent θ_m^2 vs. N^2. Red line is the linear fit to extract the thickness of the sample.</p>	8
<p>FIG. 2.1. Sketch of the geometry, the exchange bias field H_{eb} serves as a reference direction. The static external magnetic field H is applied in the film plane at an angle ϕ_H with the microwave field h_{mw} also applied in the film plane, but perpendicular to H. Also shown is the magnetization M with equilibrium orientation (θ_0, ϕ_0) and the easy axis of the (in-plane) uniaxial anisotropy field H_u, which is shown at an angle ϕ_u relative to the exchange bias direction.</p>	17
<p>FIG. 2.2. Microwave frequency f versus resonance field H_{res} (Kittel plot) for a 6 nm CoFe exchange biased layer. Black (red) symbols show broadband FMR data with the external magnetic field applied parallel (antiparallel) to the exchange bias direction. The corresponding solid lines are the result of a simultaneous fit to the Kittel Eq. (2.6) for both orientations.</p>	19
<p>FIG. 2.3. Effective magnetization M_{eff}, determined using broadband ferromagnetic resonance data, as a function of the inverse CoFe film thickness t_{CoFe}. The red line is a linear fit of the experimental data.</p>	20
<p>FIG. 2.4. Dependence on the in-plane angle of the applied field ϕ_H of (a) the resonance field H_{res} of a 6 nm CoFe exchange biased layer. The figure includes the experimental data (blue</p>	

symbols), a fit using the analytic model (green line) and a fit using the full model (red line), (b) the residuals of the fit using the analytical model (green line & symbols) and the full model (red line & symbols) and (c) the misalignment of the in-plane angle of the magnetization ϕ_0 from the direction of the applied field ϕ_H calculated using the full model.... 23

FIG. 2.5. Dependence on the in-plane angle of the applied field ϕ_H of (a) the resonance field H_{res} . The red line is the result of the full model for $H_{eb} = 500$ [Oe] and $H_u = 200$ [Oe], the green line is a fit of this data using Eq. (2.6), (b) the residuals of the fit and (c) the misalignment of the equilibrium direction of the magnetization ϕ_0 from the direction of the applied field ϕ_H 24

FIG. 2.6. Field shift H_{shift} of the magnetization reversal curves as a function of the in-plane angle ϕ_H of the applied field. Experimental data determined using the magneto-optic Kerr effect is shown as blue symbols, whereas the red line is a fit using $H_{shift}(\phi_H) = H_{eb} \cos(\phi_H)$. 26

FIG. 2.7. Exchange bias field H_{eb} as a function of the inverse of the CoFe thickness t_{CoFe} as determined from ferromagnetic resonance data (black solid symbols) and MOKE data (blue open symbols). The red line shows a linear fit of the data. The inset shows the in-plane uniaxial anisotropy field as determined from ferromagnetic resonance data as a function of the CoFe thickness. 27

FIG. 2.8. Ferromagnetic resonance linewidth ΔH as a function of the microwave frequency f for a CoFe sample with a thickness of (a) $t_{CoFe} = 4$ [nm] and (b) $t_{CoFe} = 6$ [nm]. The black (red) symbols represent broadband FMR data measured with the field parallel (antiparallel) to the exchange bias direction. The solid lines show a fit of the data assuming Gilbert-type damping, Eq. (2.8), and the dashed line in (a) shows a fit of the data assuming two-magnon scattering as described by Eq. (2.9). 29

FIG. 2.9. Effective Gilbert-type damping parameter α_{eff} as a function of the square of the inverse CoFe thickness t_{CoFe} . The black (red) symbols represent damping parameters determined from broadband FMR data measured with the field parallel (antiparallel) to the exchange bias direction. The solid lines show linear fits of the data. 30

FIG. 2.10. (a) Peak-to-peak ferromagnetic resonance linewidth ΔH as a function of the in-plane angle ϕ_H of the applied field measured for a 6 nm thick exchange biased CoFe film at a microwave frequency of $f = 20$ [GHz]. Experimental data is shown as blue symbols, the red and green lines represent fits using a unidirectional relaxation described by Eq. (2.11) using the full model and assuming $\phi_0 = \phi_H$ respectively. (b) Residuals of the two different fits. 32

FIG. 2.11. Unidirectional linewidth contribution ΔH_{eb} determined from in-plane angle dependent FMR measurements. In (a) this contribution is plotted as a function of $1/t_{CoFe}^2$, the blue line is a linear fit of the data with a vanishing unidirectional linewidth contribution for the bulk. In part (b) the same data is shown as a function of the inverse CoFe thickness t_{CoFe} . The red line is a fit including a contribution linear (dashed green line) and quadratic (dashed blue

line) in the inverse film thickness. The red shaded area indicates the 95% confidence bands of the fit. 34

FIG. 3.1. Kittel plot for Si/SiO₂/Ni_{0.8}Fe_{0.2}/SiO₂ samples. Different colors represent different Ni_{0.8}Fe_{0.2} layer thicknesses. 43

FIG. 3.2: M_{eff} vs. $1/tNiFe$ for Si/SiO₂/Ni_{0.8}Fe_{0.2}/SiO₂ (blue symbols), Si/SiO₂/Ni_{0.8}Fe_{0.2}/Ru (red symbols), and Si/SiO₂/Ru/Ni_{0.8}Fe_{0.2}/Ru (green symbols). The lines are the fit to each data set. 45

FIG. 3.3. Effective Gilbert damping vs. $1/tNiFe$ for Si/SiO₂/Ni_{0.8}Fe_{0.2}/SiO₂ (blue symbols), Si/SiO₂/Ni_{0.8}Fe_{0.2}/Ru (red symbols), and Si/SiO₂/Ru/Ni_{0.8}Fe_{0.2}/Ru (green symbols). 46

FIG. 3.4. Linewidth vs. elevation angle for Si/SiO₂/Ni_{0.8}Fe_{0.2} (6nm)/SiO₂ (blue symbols), Si/SiO₂/Ni_{0.8}Fe_{0.2} (6nm)/Ru (red symbols), and Si/SiO₂/Ru/Ni_{0.8}Fe_{0.2} (6nm)/Ru (green symbols). The microwave frequency was 20 GHz. 47

FIG. 4.1. (a) Periodic checkerboard pattern used for the simulations, regions A have a second-order perpendicular anisotropy $K_{2,A} = -1.5 \times 10^6 J/m^3$ whereas for regions B $K_{2,B} \geq 0$. (b) Relaxed magnetization with an external magnetic field of $\mu_0 H = 1T$ applied at an angle of $\theta_H = 5^\circ$ with respect to the film normal. 55

FIG. 4.2. Dependence of (a) the total energy density, (b) the demagnetizing energy density, (c) the anisotropy energy, (d) the exchange energy density and (e) the Zeeman energy density on the average magnetization angle θ_M obtained after relaxing the magnetization with the indicated external magnetic field applied at different angles. The solid lines are a fit using the macrospin model, see Eq. (4.3). The dashed lines in (b) and (c) represent the expected angular dependence for the demagnetizing energy density of an infinite thin film and the volume averaged anisotropy energy density respectively. 57

FIG. 4.3. (a) Deviation of the average angle of the magnetization θ_M from the angle of the applied field θ_H shown as a function of the average angle of the magnetization θ_M . The symbols represent the results from micromagnetic simulations with different strengths of the applied field. The red dash dotted line is the result obtained by ignoring exchange interaction and treating each region as a separate macrospin for an applied field $\mu_0 H = 5T$. (b) Standard deviation H_{θ_M} of the magnetization angle from its average orientation θ_M as a function of the same. The symbols represent the results from micromagnetic simulations with different strengths of the applied field. The red dash dotted line is the result obtained by ignoring exchange interaction and treating each region as a separate macrospin for an applied field $\mu_0 H = 5T$, here the difference between the angle of the magnetization in region A and B is shown. 59

FIG. 4.4. (a) Field dependence of the effective second-order uniaxial anisotropy determined by fitting Eq. (4.3) to the angular dependence of the different contributions to the total energy, cp. Fig. 4.2. The dashed red line is the volume averaged second-order uniaxial anisotropy. The pink dashed line represents the demagnetization energy density for a homogeneously

magnetized infinite film. The dash dotted red line is the anisotropy contribution to the effective second-order uniaxial anisotropy obtained by ignoring exchange interactions between the regions and treating them each as a macrospin. The dark red dash dotted line is the Zeeman contribution to the effective second-order anisotropy using the same simplified model. (b) Field dependence of the effective fourth-order uniaxial anisotropy. The dash dotted red lines represent contribution obtained by ignoring exchange interactions between the regions and treating them each as a macrospin, the anisotropy and Zeeman contribution are shown in red and dark red respectively. The blue symbols in both graphs are the effective anisotropies determined from dynamical calculations, see section 4.II.D. 60

FIG. 4.5. (a) Dependence of the effective second-order uniaxial anisotropy on the lateral length scale of the second-order anisotropy variations. The dashed red line is the volume averaged second-order uniaxial anisotropy. The pink dashed line represents the demagnetization energy density for a homogenously magnetized infinite film. The dash dotted red line is the anisotropy contribution to the effective second-order uniaxial anisotropy obtained by ignoring exchange interactions between the regions and treating them each as a macrospin. The dark red dash dotted line is the Zeeman contribution to the effective second-order anisotropy using the same simplified model. The black dash dotted line is the sum of demagnetization energy, the anisotropy and Zeeman contribution in the macrospin approximation. (b) Dependence of the effective fourth-order uniaxial anisotropy on the lateral length scale of the second-order anisotropy variations. The dash dotted red lines represent contribution obtained by ignoring exchange interactions between the regions and treating them each as a macrospin, the anisotropy and Zeeman contribution are shown in red and dark red respectively. The black dash dotted line is the sum of these contributions. The gray vertical dashed lined is the length scale λ_{eff} , see text for details. 66

FIG. 4.6. Sketch of the configuration for determining the dynamic properties of the system. In (a) the out-of-plane configuration and in (b) the in-plane configuration is shown. The small additional field h_p is only present during relaxation of the initial state and is removed at $t=0$ 69

FIG. 4.7. (a) Time evolution of the average magnetization components M_x and M_y for a 20nm x 20nm structure with $K_{2,A} = -1.5 \times 10^6 J/m^3$ and $K_{2,B} = 0 J/m^3$ with an external magnetic field of $\mu_0 H = 2T$ applied along the film normal $\theta_H = 0^\circ$. The inset shows the time evolution during the first tenth of a nanosecond. (b) Shows $P(M_y)$, i.e. the power spectral density of the y -component of the magnetization averaged over all cells in the simulation volume for the same parameters as in (a). The insets of this figure show the power spectral density maps for the first three resonances at frequencies $f_{\perp 1} = 54.9$ GHz (fundamental resonance mode), $f_{\perp 2} = 184$ GHz and $f_{\perp 3} = 288$ GHz. Here the color indicates the contribution of each cell to the power spectral density, with dark red indicating the largest and dark blue zero contribution. 69

FIG. 4.8. (a) Dependence of the contribution of region A to the total power spectral density of the fundamental mode on the lateral length scale L_x, y of the variations of the anisotropy. (b)-(d) show spectral maps with the static field applied in-plane whereas (e)-(g) show

spectral maps with the static field applied out-of-plane. For (b) & (e) $L_x = L_y = 10 \text{ nm}$, for (c) & (f) $L_x = L_y = 20 \text{ nm}$ and for (d) & (g) $L_x = L_y = 60 \text{ nm}$ 70

FIG. 4.9. Effective second-order uniaxial anisotropy as a function of the lateral length scale Lx, y of the variations of the anisotropy. The anisotropy $K_{2,eff}^{dyn}$ for the dynamic simulations is shown as blue symbols whereas the anisotropy $K_{2,eff}$ determined from quasi-static simulations is shown as black symbols. The dashed black line shows the thin film limit with an average anisotropy, i.e. $\mu_0 M_s^2 / 2 + K_{2,A} + K_{2,B}$. The dashed blue line represents the large length scale limit for the dynamical simulations $\mu_0 M_s^2 / 2 + K_{2,A}$. (b) Effective fourth-order uniaxial anisotropy as a function of the lateral length scale Lx, y of the variations of the anisotropy. The anisotropy $K_{4,eff}^{dyn}$ for the dynamic simulations is shown as blue symbols whereas the anisotropy $K_{4,eff}$ determined from quasi-static simulations is shown as black symbols. The dashed blue line represents the large length scale limit for the dynamical simulations $K_{2,B} - K_{2,A}$. In both figures the dash dotted black lines are the limiting values expected for the quasi-static effective anisotropies, obtained by treating each region as a macrospin and ignoring exchange interaction, see section C. 73

1. INTRODUCTION

I. Magnetization dynamics

Magnetization dynamics in ferromagnetic systems is described by the Landau-Lifshitz-Gilbert (LLG) equation [1,2] (Equation (1.1)). In this equation, two main contributions to the time derivative of the magnetization vector are the precession term $(-\gamma\vec{M} \times \vec{H}_{eff})$ and the damping term $(\frac{\alpha}{M}\vec{M} \times \frac{\partial\vec{M}}{\partial t})$ as shown in Eq. (1.1). The precession term describes the magnetization dynamics for a system with no magnetic energy loss during the precession. However, in real systems magnetic energy is dissipated within the system. This implies the importance of the damping term in describing the more realistic precessional motion of the magnetization. Eq. (1.1) can be expanded [3] or written in different forms [4]. However, for the purpose of this dissertation the current form is the most suitable form [5]:

$$\text{LLG: } \frac{\partial\vec{M}}{\partial t} = -\gamma\vec{M} \times \vec{H}_{eff} + \frac{\alpha}{M}\vec{M} \times \frac{\partial\vec{M}}{\partial t} \quad (1.1)$$

In the LLG equation, \vec{M} is the magnetization vector, \vec{H}_{eff} is the effective magnetic field, α is the dimensionless Gilbert damping parameter (or simply damping parameter), and γ is the gyromagnetic ratio. \vec{H}_{eff} is the effective internal field, including the external magnetic field, the demagnetizing field, and contributions from exchange, anisotropy, and magnetoelastic effects [1].

The LLG equation can be linearized and solved to find the dispersion relation, or the Kittel equation, for the magnetic system [5]. When the applied quasi-static field is in the plane of the film, the dispersion relation for a thin ferromagnetic (FM) film can be written as in Eq. (1.2):

$$f = \gamma' \sqrt{H_{res}(H_{res} + \xi M_{eff})}. \quad (1.2)$$

In Eq. (1.2), f is the frequency of precessional motion of the magnetization, H_{res} is the resonance field, γ' is $\gamma/2\pi$, and M_{eff} is the effective magnetization. ξ is a notation introduced by Brown [6,7] to include different systems of units. In particular, $\xi = 1$ for SI units and $\xi = 4\pi$ for the Gaussian or CGS units. f is in Hz (1/second or 1/s) in both unit systems, H_{res} is in Ampere/meter or A/m (Orsted or Oe) in SI (CGS) unit system. γ' is in m/As (Hz/Oe), and M_{eff} is in A/m (electromagnetic unit/centimeter³ or emu/cm³) in SI (CGS).

If the quasi-static field is applied perpendicular to the film plane (out-of-plane configuration), the dispersion relation is written as in Eq. (1.3).

$$f = \gamma'(H_{res} - \xi M_{eff}). \quad (1.3)$$

M_{eff} is defined in Eq. (1.4).

$$\xi M_{eff} = \xi M_s - \frac{2K_u}{\mu_0 M_s}. \quad (1.4)$$

In equations (1.4) K_u is the perpendicular anisotropy constant, M_s is the saturation magnetization of the ferromagnetic material, and $\mu_0 = 4\pi \times 10^{-7} H$ ($\mu_0 = 1$) is the vacuum permeability in SI (CGS) units.

The effective magnetization is introduced in the dispersion relation due to the presence of the demagnetizing field and the uniaxial perpendicular anisotropy field. From the magnetic energy point of view, one can see that demagnetizing energy and uniaxial perpendicular

anisotropy energy have the same angular dependence. Therefore, separation between the two terms is not possible even by performing angular dependent measurements. However, in certain cases it is possible to separate the two terms because they have different thickness dependence as discussed in detail in chapter three.

The form of the dispersion relation shown in equations (1.3) and (1.4) is the simplest form for a thin film. For magnetic structures with magnetocrystalline anisotropy, exchange bias effect [8,9], etc. the dispersion relation needs to include additional terms. In another common approach, the dispersion relation for a desired system is derived by writing the energy functional and minimizing it to find the equilibrium condition for the magnetization. In the next step, the Smit-Beljers formula [10] is used to write the Kittel equation. However, in general it is not possible to find the analytical solution to the energy minimization. A few assumptions are often used to approximate the solution. The most common approximation is to assume that the magnetization is always perfectly aligned with the applied quasi-static magnetic field. This method is used in chapter two for a system with a strong exchange bias anisotropy and an additional uniaxial anisotropy. In chapter two, the numerical solution is provided and compared to the analytical solution with mentioned approximation.

II. Experimental procedure

A. Ferromagnetic resonance technique

Experimentally, the magnetization dynamics of a system can be studied by utilizing various techniques such as Brillouin Light Scattering (BLS) [11] and Ferromagnetic Resonance (FMR) [12]. In this dissertation FMR is used as a powerful tool to investigate dynamic properties of thin magnetic films. In a typical FMR experiment, a quasi-static magnetic field \vec{H} is applied to

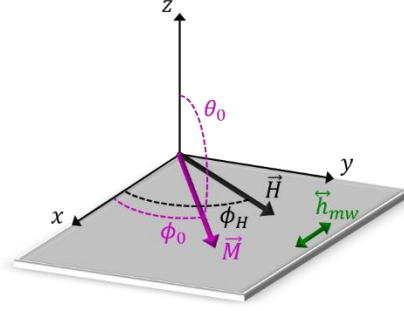


FIG 1.1. Schematics of the applied quasi-static field \vec{H} , microwave field \vec{h}_{mw} , and the magnetization \vec{M} for a ferromagnetic thin film in the xy plane. In general, the magnetization vector is not aligned with the applied field. ϕ_0 and θ_0 are the azimuthal angle of the magnetization vector (measured from x axis) and the polar angle of the magnetization vector (measured from z axis), respectively. ϕ_H and θ_H represent the azimuthal and polar angle of \vec{H} , respectively.

the thin film. In addition, a small time-dependent microwave magnetic field \vec{h}_{mw} (with frequency f in the GHz range) is applied perpendicular to the quasi-static field (see Fig. 1.1).

The quasi-static field \vec{H} is then swept through the resonance field H_{res} , e.g. the applied field at which the resonance condition is met, at a fixed microwave frequency f . In experiment the derivative of the imaginary part of the susceptibility with respect to H is measured, as FMR spectra, varying the applied field strength H at constant frequency. A least square fit method is used to fit the FMR data to a first derivative of a Lorentzian line shape [13,14], as shown in Eq. (1.5):

$$y = \frac{a\left(\frac{H_{res}-H}{\Delta H}\right) + 9b - 3b\left(\frac{H_{res}-H}{\Delta H}\right)^2}{\left[3 + \left(\frac{H_{res}-H}{\Delta H}\right)^2\right]^2}. \quad (1.5)$$

In this equation a is the absorption amplitude, and b is the dispersion term amplitude. From this fit, one can obtain H_{res} and the peak-to-peak linewidth ΔH as shown in Fig. 1.2. Performing FMR experiments over a broad frequency range and fitting the obtained f vs. H_{res} data to the dispersion relation (Kittel equation) allows one to obtain magnetic parameters such as

M_{eff} , γ' , anisotropy fields, etc. precisely [15]. Moreover, the ΔH vs. f analysis allows one to study

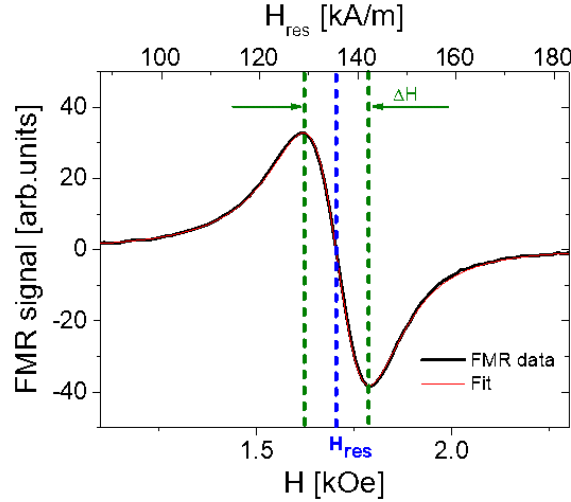


FIG 1.2. A typical raw FMR data at a fixed frequency. The black line shows the experimental FMR data and the red line is the fit to Eq. (1.5).

the relaxation processes in magnetic structures. For systems for which Gilbert damping is the main relaxation mechanism the FMR linewidth is strictly linearly dependent on the microwave frequency and this allows us to obtain the Gilbert damping parameter using Eq. (1.6) [16,17]:

$$\Delta H = \Delta H_0 + \frac{2}{\sqrt{3}} \frac{\alpha}{\gamma'} f. \quad (1.6)$$

In this equation α is the Gilbert damping parameter and ΔH_0 represents the inhomogeneous linewidth broadening that is caused by defects, imperfections, etc. and it is very sensitive to the thermal history of the material [16]. It is worth mentioning that the frequency dependence of ΔH is not always linear but can be more complicated when the relaxation mechanism in the sample is not only Gilbert damping but includes other processes such as two-magnon scattering (TMS). This is discussed more in detail in chapter two.

FMR results for this dissertation are performed using an in-house developed setup shown in Fig. 1.3. A quasi-static magnetic field is provided by an electromagnet that can create

magnetic fields up to 1.8 T. The time dependent magnetic field is provided by a microwave source with a frequency range of 2-70 GHz. Up to 20 dBm microwave power can be delivered to the sample and the transmitted power is collected by a microwave diode. When the FMR condition is met at a specific frequency, the drop in transmitted microwave power is measured as FMR signal. A Lock-in technique [18] is used to measure the FMR signal with high sensitivity. In this setup the absolute value of the amplitude and the phase can be measured simultaneously. To use the lock-in technique, the signal is modulated with fields as high as 40 Oe using two coils that are attached to the pole pieces. This setup is controlled by a computer and is fully automated. Moreover, this system has the capability to perform precise angular dependent measurements allowing to study in-plane anisotropy as well as to perform elevation angle measurements.

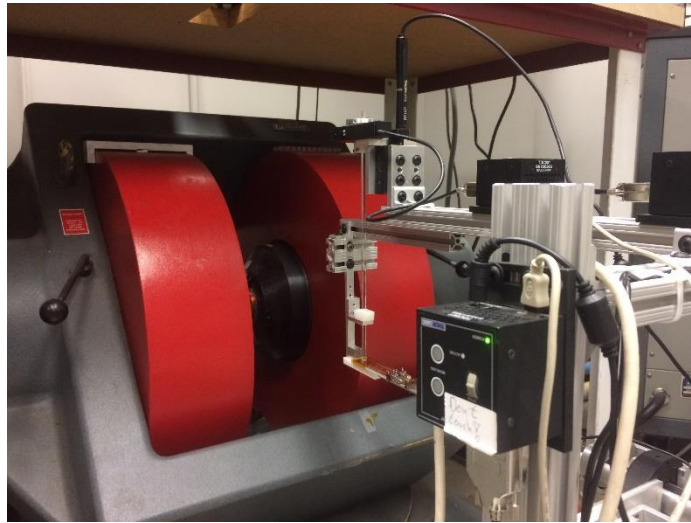


FIG. 1.3. Broadband ferromagnetic resonance (FMR) setup. The setup is capable of performing polar (θ), and azimuthal (ϕ) angular dependent measurements.

B. Magnetron sputtering

Alternative current (AC) and radio frequency (RF) magnetron sputtering methods are used to fabricate the samples for which the results are presented in chapter three. This technique is widely used in industry and research centers due to the compatibility of the setup to deposit

metallic as well as non-metallic thin films. Other than textured samples [19], post deposition techniques, such as annealing, allows researchers to prepare single crystal thin films [20]. In this technique, the target is hit by the ionized gas (argon) atoms. As a result, ions are sputtered from the target and land on the substrate. To increase the sputtering efficiency in magnetron sputtering a local magnetic field is used to define a spiral trajectory for ions.

The sputtering system, which is used to deposit samples for this research, is equipped with four guns that can be connected to both AC and RF power supply. Twelve samples can be deposited in one round, which is important to keep the deposition condition consistent for sample series that are used in chapter three. These capabilities made it possible to deposit multilayers of metallic and non-metallic materials without breaking the vacuum. The vacuum is monitored during the pump down and baking, using a mass spectrometer. The pressure of the chamber can reach down to 10^{-7} torr prior to baking, and a light bulb was used to bake the system for eight hours to reach a base pressure of 10^{-8} torr. The deposition rate is monitored using a quartz crystal. In addition, calibration samples are made to find and optimize the deposition rate for each target. Further optimizations are performed to assure depositing multilayers with very smooth surfaces and interfaces.

C. X-Ray reflectivity experiment

X-Ray reflectivity (XRR) and X-Ray diffraction (XRD) experiments are performed for thickness measurements as well as crystallography studies.

In the XRR experiment, the X-Rays are incident on the sample under a small angle θ and the diffracted beam is measured by the detector after specular reflection. The angle θ is varied to obtain intensity (counts per second) vs. θ , shown in Fig. 1.4 ,and θ_m angles that are θ values at which the intensity has a local maxima.

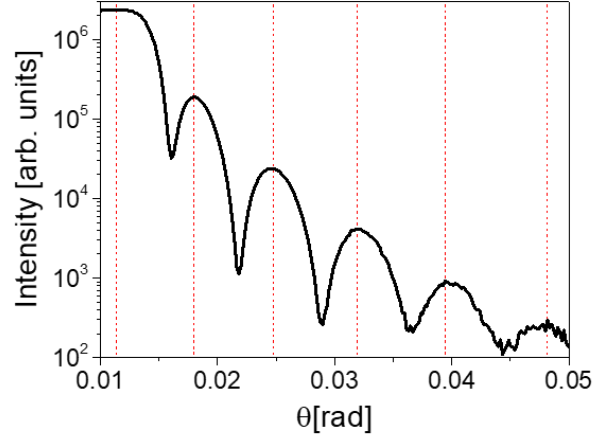


FIG. 1.4. A typical XRR data. Intensity (counts) is plotted vs. angle θ in range of 0.01 rad to 0.05 rad. Dashed lines correspond to local intensity maxima where $\theta = \theta_m$.

The thickness of the thin films are calculated fitting θ_m vs. N^2 using Eq. (1.7) as shown in

Fig. 1.5 [21]:

$$\theta_m^2 = \left(\frac{\lambda}{2d}\right)^2 N^2 + \theta_c^2. \quad (1.7)$$

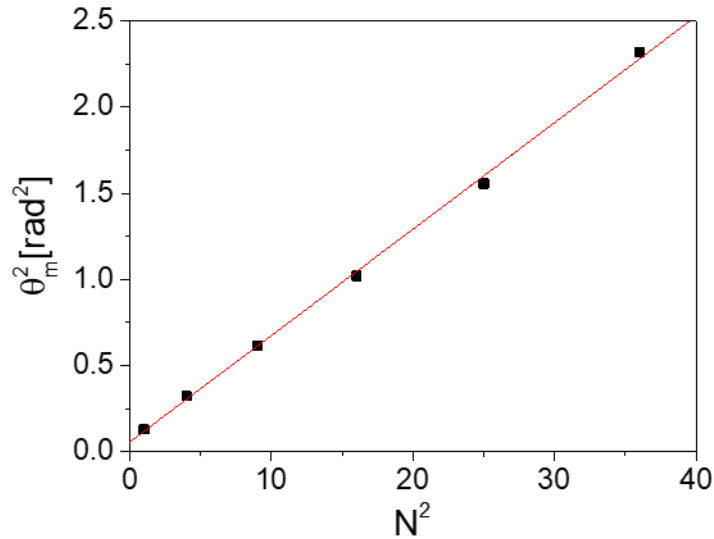


FIG. 1.5. Symbols represent θ_m^2 vs. N^2 . Red line is the linear fit to extract the thickness of the sample.

In this equation, d is the film thickness, N is the number of the peak ($N = 1$ represent the first peak, for the second peak $N = 2$, etc.) and θ_c is the critical angle. λ is the wavelength of the X-Ray source, which is 0.15406 nm for Cu- $K_{\alpha 1}$.

III.Micromagnetic simulations

Micromagnetic simulations enable us to investigate the magnetization dynamics in ferromagnetic thin films and multilayers on length scales larger than the atomic spacing. Using this method, it is possible to study the magnetic energy landscape. This allows to obtain a fundamental understanding of the interplay between various interactions and how these interactions result in a specific measurable effect. The in-house developed MATLAB-based code M^3 [22] is used for all of the simulations that are presented in this dissertation. The magnetic structure is comprised of right rectangular prisms of desired size. The code allows to use a macrospin model as well as full micromagnetic simulations. It serves as a powerful tool to investigate the accuracy of the macrospin model in describing the magnetic energy and magnetic interactions within the system. For simulations that are presented in this dissertation, LLG equation was solved considering the main interactions that are present in the particular system, i.e. Zeeman, anisotropy, demagnetizing, and exchange interactions are included. For the exchange anisotropy, the six-neighbor method is used with the Neuman boundary condition. The periodic boundary condition can be applied to simulate an infinitely large thin film. Magnetic parameters of individual cells can be set to study various interactions performing full micromagnetic simulations. The time and spatial dependence of the magnetization is then studied for a given system. In chapter four and appendix one, results of micromagnetic simulations for two systems are discussed. In all of these simulations the length scale of the system is smaller than that of magnetic domains.

IV. Magnetic anisotropy and relaxation study

Various types of magnetic anisotropy are controlled and utilized in magnetic sensors [23] as well as in devices to read and store data. The exchange bias effect [8,9] and interfacial perpendicular anisotropy (PMA) [24,25] are frequently used in magnetic systems for a broad range of applications. In this work, ferromagnetic resonance studies and micromagnetic simulations are used to study the magnetic anisotropy and magnetic relaxation in multilayered structures.

The exchange bias anisotropy can be present in an antiferromagnetic/ferromagnetic (AF/FM) bilayer. In these systems the FM layer is pinned to the AF at the interface. As a result, the magnetization dynamics and magnetic relaxation in the FM layer is affected by the FM-AF coupling. In chapter two [26], exchange bias anisotropy and magnetic damping is discussed for a system in which exchange bias and interfacial PMA coexist. Studying magnetic relaxation in a system with exchange bias anisotropy using the broadband FMR technique confirms the unidirectional nature of the magnetic damping [27,28], which is consistent with the previously reported uniaxial relaxation mechanism [27]. The thickness dependence of the damping suggests that Two-Magnon Scattering (TMS) contributes significantly to the relaxation. However, our precise angular dependent FMR measurements reveal that in addition to an inverse thickness-square dependence of the magnetic damping there is another unidirectional relaxation mechanism that scales with the inverse of the FM layer thickness. In addition to anisotropy and relaxation analysis in exchange bias systems, fitting the angular dependence of the ferromagnetic resonance field indicates a fairly large misalignment between the magnetization and the magnetic field.

Interfacial PMA is another form of anisotropy that is studied in this work. The increasing need for PMA encourages, and urges, scientists to search for materials and structures in which this form of anisotropy is enhanced. It is both intriguing and challenging to explore such systems because of their applications in many spintronic devices such as Magnetic Tunnel Junctions (MTJs). This is, in part, due to the fact that the origin of PMA is not well understood [29]. However, hybridization of atomic orbitals at the interface is known to play a significant role in enhancing PMA. First principle calculations (see appendix two), and experimental methods are two tools to achieve this goal. Theoretical investigations are needed to predict and optimize PMA. Moreover, fabrication and characterization of thin films with a large PMA is possible through many deposition methods such as sputtering, physical vapor deposition, chemical vapor deposition, molecular beam epitaxy, etc. In chapter three [30], interfacial PMA is studied in $\text{Ni}_{0.8}\text{Fe}_{0.2}$ thin films in proximity of Ru and SiO_2 layers. FMR studies confirm the presence of interfacial PMA that originate from $\text{Ni}_{0.8}\text{Fe}_{0.2}/\text{Ru}$ and $\text{Ni}_{0.8}\text{Fe}_{0.2}/\text{SiO}_2$ interfaces.

However, magnetic anisotropy in multilayers with uniaxial PMA is not perfectly homogeneous. Morphology at the interface or slight spatial variations in stoichiometry can lead to spatial variations in the strength of interfacial PMA. The spatial variations lead to the presence of a higher order anisotropy. This effect can be observed experimentally in systems with strong uniaxial PMA [15]. Quasi-static methods such as torque magnetometry can give insights from the magnetic energy point of view. In addition, this effect can be investigated through dynamic methods such as FMR technique. However, inconsistencies between the static and dynamic method results are expected due to the different nature of the two techniques. Higher order anisotropy in systems with fluctuating uniaxial anisotropy is investigated in chapter four [31] by micromagnetic simulations.

Spatial fluctuations of the uniaxial PMA are simulated using a checkerboard pattern which is comprised of regions A and B in which uniaxial PMA is K_A and K_B , respectively. The angular dependence of shape anisotropy, uniaxial PMA, Zeeman, and exchange anisotropy and the total magnetic energy of these interactions are investigated to study the individual contribution of each interaction to the overall higher order anisotropy. The dependence of these contributions on the applied magnetic field and length scale of the fluctuations are also studied in detail. In addition, dynamical response of the system approves the presence of higher order anisotropy in this system.

In the next three chapters, exchange bias anisotropy, uniaxial PMA, and higher order anisotropy in systems with inhomogeneous uniaxial PMA are discussed in detail. Relaxation analyses in these systems are reported in detail. In chapter five, this research is summarized and concluded, and suggestions for further studies are presented.

2. BROADBAND FERROMAGNETIC RESONANCE CHARACTERIZATION OF ANISOTROPIES AND RELAXATION IN EXCHANGE BIASED IrMn/CoFe BILAYERS

Jamileh Beik Mohammadi*^{1,2}, Joshua Michael Jones^{1,2}, Soumalya Paul^{1,2}, Behrouz Khodadadi^{1,2},
Claudia K.A. Mewes^{1,2}, Tim Mewes^{1,2}, Christian Kaiser³

1: Center for Materials for Information Technology, University of Alabama, Tuscaloosa, Alabama 35487

2: Department of Physics and Astronomy, University of Alabama, Tuscaloosa, Alabama 35487

3: Western Digital, Fremont, California, 94539

The magnetization dynamics of exchange-biased IrMn/CoFe bilayers have been investigated using broadband and in-plane angle-dependent ferromagnetic resonance spectroscopy. The interface energy of the exchange bias effect in these bilayers exceeds values previously reported for metallic antiferromagnets. A strong perpendicular magnetic anisotropy and a small in-plane uniaxial anisotropy are also observed in these films. The magnetization relaxation of the bilayers has a strong unidirectional contribution, which is in part caused by two-magnon scattering. However, a detailed analysis of in-plane angle- and thickness-dependent linewidth data strongly suggests the presence of a previously undescribed unidirectional relaxation mechanism.

I.Introduction

Since the discovery of the exchange bias effect by Meiklejohn and Bean in 1956 [1,2], this topic has remained a very active research area. This is due in part to the many practical applications of this effect in data storage devices. In recent years, the exchange bias effect has been of particular importance for pinning the reference layer in spin valve structures [3], which are used, for example, in read heads and spin transfer torque magnetic random access memories [4,5]. Another reason for the continued interest in this topic is the inherent complexity of the competing interactions at the interface between a ferromagnet and an antiferromagnet [6], which leads to very rich physics [7]. A particularly interesting feature, not only for future applications, but also for obtaining new insights into the underlying physics, is the influence of the exchange bias effect on the magnetization dynamics of the ferromagnet [8,9]. One of the most prominent features of the exchange bias effect is that it leads to a preferred direction of the magnetization (unidirectional anisotropy) of the bilayer system. This easy direction of the unidirectional anisotropy is typically established during annealing and subsequent cooling in an applied magnetic field. The unidirectional anisotropy manifests itself in a shift or “bias” of the magnetization reversal curve on the magnetic field axis. However, magnetization reversal measurements can be difficult to analyze quantitatively, in particular, due to the complex phase diagrams [10,11] and the formation of complicated domain structures [12–15]. Here, measurements of the magnetization dynamics, for example, using ferromagnetic resonance [8,16–18] or Brillouin light scattering [17–19], offer the advantage that they can be carried out at external magnetic fields sufficient to saturate the system. While most of the early work on magnetization dynamics of exchange-biased systems focused on the determination of the unidirectional anisotropy to provide input to model development, it was also noted early on that

the exchange bias effect has a profound influence on the magnetization relaxation in these systems [16,18]. Two-magnon scattering at the ferromagnet/antiferromagnet interface is one of the major contributions to the relaxation in these systems [9,17,20]. However, it was only after the development of broadband ferromagnetic resonance capabilities that a unidirectional contribution to the relaxation in these systems was observed [21]. In the present paper, we utilize broadband ferromagnetic resonance to investigate the magnetization dynamics in the IrMn/CoFe exchange-biased system to precisely determine anisotropies. By investigating the CoFe thickness and in-plane angle dependencies, we are able to show that this system has a strong interfacial perpendicular anisotropy in addition to the very strong interfacial exchange coupling. We further show that the magnetization relaxation in this system has a very strong unidirectional contribution, which is in part caused by two-magnon scattering. However, we also present evidence that the strong unidirectional relaxation in this system deviates from the expected thickness dependence of a strictly interfacial two-magnon scattering contribution. Our analysis therefore suggests the presence of a previously undescribed unidirectional relaxation mechanism in this system. The chapter is organized as follows. In Sec. 2.II, we describe the experimental procedures used to characterize the samples. In Sec. 2.III, we summarize the models commonly used to describe ferromagnetic resonance in exchange-biased systems. Section 2.IV describes the results regarding the magnetic anisotropies present in the IrMn/CoFe exchange biased system. In Sec. 2.V, we describe in detail the results regarding the strong unidirectional magnetization relaxation observed in this system. The paper concludes with a summary in Sec. 2.VI.

II.Experimental procedures

The samples were prepared with an Anelva sputter deposition system onto SiO₂ substrates with the following layer sequence: SiO₂/Ta (2 nm)/Ru (3 nm)/ IrMn (6 nm)/CoFe

(t)/Ru (3 nm)/Ta (2 nm)/Ru (5 nm). CoFe layer thickness t ranged from 2 to 20 nm. In order to set the exchange bias direction, the samples were annealed at 285°C for 5 hours in an applied field of 5 T. The IrMn thickness of 6 nm is significantly larger than the critical thickness of this antiferromagnet, thereby ensuring saturation of the exchange bias effect [22].

The quasistatic magnetic properties of the samples were determined using magneto-optical Kerr effect(MOKE) measurements, whereas the dynamic properties were determined using broadband ferromagnetic resonance spectroscopy (FMR) covering a frequency range from 2 to 64 GHz. In both cases, the samples were measured at room temperature. For broadband FMR measurements, the external field was oriented parallel and antiparallel to the exchange bias direction. In addition, we also carried out in-plane angle-dependent measurements at selected frequencies to obtain additional information about the magnetic anisotropies and the relaxation mechanisms of the samples. The raw spectroscopy data were analyzed by fitting a Lorentzian peak profile including both dispersive and absorptive components in order to extract the resonance field, H_{res} , and the peak-to-peak linewidth, ΔH , at each frequency [23,24].

III. Ferromagnetic resonance in exchange bias system

In FMR measurements the resonance condition can be derived using the Smit and Beljers relation [25]:

$$\left(\frac{\omega}{\gamma}\right)^2 = \frac{1}{M_s \sin^2 \theta} \left[\frac{\partial^2 F}{\partial \theta^2} \frac{\partial^2 F}{\partial \phi^2} - \left(\frac{\partial^2 F}{\partial \theta \partial \phi} \right)^2 \right] \quad (2.1)$$

where $\omega = 2\pi f$ is the angular frequency of the microwave field, M_s is the saturation magnetization, γ the gyromagnetic ratio, θ the polar angle of the magnetization with respect to the normal of the film, and ϕ the azimuthal angle of the magnetization, for which we choose the exchange bias direction as a reference, i.e. $\phi_{eb} = 0$. The free energy F of the ferromagnet in the exchange bias system includes Zeeman, demagnetizing, exchange bias, and uniaxial anisotropy

terms. The last two contributions are characterized by the exchange bias field H_{eb} and the uniaxial anisotropy field $H_u = \frac{2K_u}{M_s}$.

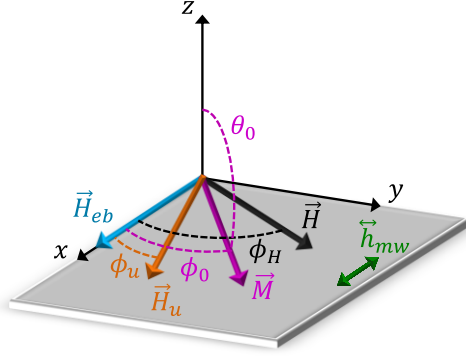


FIG. 2.1. Sketch of the geometry, the exchange bias field \vec{H}_{eb} serves as a reference direction. The static external magnetic field \vec{H} is applied in the film plane at an angle ϕ_H with the microwave field \vec{h}_{mw} also applied in the film plane, but perpendicular to \vec{H} . Also shown is the magnetization \vec{M} with equilibrium orientation (θ_0, ϕ_0) and the easy axis of the (in-plane) uniaxial anisotropy field \vec{H}_u , which is shown at an angle ϕ_u relative to the exchange bias direction.

Equation (2.1) is evaluated at the equilibrium (θ_0, ϕ_0) of the magnetization for which

$$\left. \frac{\partial F}{\partial \theta} \right|_{\theta_0} = 0 \quad , \quad \text{and} \quad \left. \frac{\partial F}{\partial \phi} \right|_{\phi_0} = 0 \quad (2.2)$$

In its most general form Eq. (2.3) does not have an analytical solution, but can be readily solved numerically. To obtain further insights, analytical solutions are frequently obtained by assuming that the equilibrium direction of the magnetization coincides with the direction (θ_H, ϕ_H) of the external magnetic field, i.e.

$$\theta_0 = \theta_H \quad , \quad \text{and} \quad \phi_0 = \phi_H \quad (2.3)$$

However, it is important to point out that while this assumption may be valid along high symmetry directions it is generally not a good approximation even for large external fields when the external magnetic field is applied at an arbitrary angle (see the discussion in section B.1). If one further assumes that the external magnetic field is applied in the plane of the film ($\theta_H = 90^\circ$) and that the easy axis of the uniaxial anisotropy coincides with the easy direction of the

exchange bias effect ($\phi_u = \phi_{eb} = 0$) one has for the dispersion relation (cp. for example reference [26]):

$$\left(\frac{\omega}{\gamma}\right)^2 = [4\pi M_{eff} + H_u \cos^2(\phi_H) + H_{res} + H_{eb} \cos(\phi_H)] \cdot [H_u \cos(2\phi_H) + H_{res} + H_{eb} \cos(\phi_H)] \quad (2.4)$$

In which $4\pi M_{eff}$ is the effective magnetization (the sum of demagnetizing field and the perpendicular interfacial anisotropy field), H_{res} is the resonance field, and ϕ_H is the azimuthal angle of the applied static magnetic field with respect to the exchange bias direction.

When the external magnetic field is applied parallel ($\phi_H = 0^\circ$) and antiparallel ($\phi_H = 180^\circ$) to the exchange bias direction Eq. (2.4) results in:

$$f = \frac{\gamma}{2\pi} \sqrt{[4\pi M_{eff} + H_u + H_{res} \pm H_{eb}] \cdot [H_u + H_{res} \pm H_{eb}]} \quad (2.5)$$

where the positive (negative) sign corresponds to the parallel (antiparallel) orientation. For these two configurations the external magnetic field is applied along high symmetry directions of the system and thus for sufficiently large fields the magnetization will be aligned with the field direction. Therefore, this equation can be used to fit broadband FMR data to extract the exchange bias field, the uniaxial anisotropy field, the effective magnetization and the gyromagnetic ratio.

Similarly, one can obtain an approximation for the in-plane angular dependence, which for exchange biased systems with a uniaxial anisotropy in the in-plane configuration is commonly given as [8,27]:

$$H_{res} = H_0 + H_{eb} \cos(\phi_H) + H_u' \cos(2\phi_H) \quad (2.6)$$

where H_0 is the resonance field for the measurement microwave frequency in the absence of a unidirectional and uniaxial anisotropy. The use of an analytic function to describe the angular dependence of the resonance field can simplify the data analysis significantly. However, as will

be shown below, this approximation can cause systematic variations of the residuals of the fit to experimental in-plane rotation data. In particular we will show that the underlying approximations that were used to derive Eq. (2.6) will lead to the appearance of an unphysical three-fold symmetry in the residuals of the fit to H_{res} vs. ϕ_H data. We further would like to point out that the parameter H_u' used in Eq. (2.6) to describe the uniaxial component of the resonance field should not be confused with the uniaxial anisotropy field H_u [28,29].

IV. Magnetic anisotropies

A. Broadband FMR characterization

For the exchange biased thin films, broadband FMR measurements were performed with the static external magnetic field applied parallel and antiparallel to the exchange bias direction. As shown in Fig. 2.2 for a 6 nm *CoFe* layer the field dependence of the resonance frequency is well described by Eq. (2.5). In this figure we have fitted both data sets simultaneously to obtain a consistent set of fitting parameters that minimize the sum of the squared residuals.

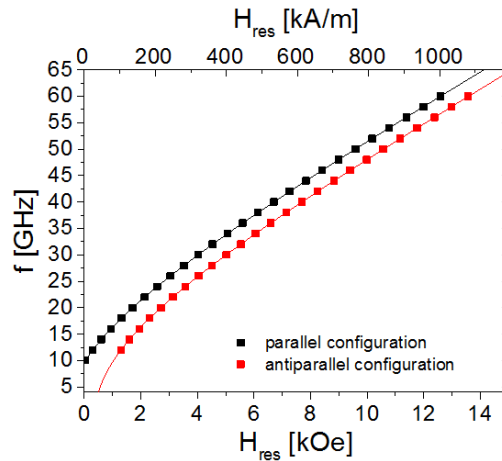


FIG. 2.2. Microwave frequency f versus resonance field H_{res} (Kittel plot) for a 6 nm CoFe exchange biased layer. Black (red) symbols show broadband FMR data with the external magnetic field applied parallel (antiparallel) to the exchange bias direction. The corresponding solid lines are the result of a simultaneous fit to the Kittel Eq. (2.6) for both orientations.

By using this approach broadband ferromagnetic resonance data can provide precise values for the effective magnetization, M_{eff} , and the gyromagnetic ratio, γ [30]. As shown in Fig. 2.3 the effective magnetization for the samples in this series shows an inverse CoFe thickness dependence with a negative slope, indicative of an interfacial perpendicular anisotropy. Assuming that there is no bulk perpendicular anisotropy present in CoFe one can determine the saturation magnetization from this graph as $M_S = 1625 \pm 25$ [emu/cm³], this value is consistent with results obtained using vibrating sample magnetometry. The slope is proportional to the interfacial perpendicular anisotropy, which in this sample series is $K_i = 1.94 \pm 0.14$ [erg/cm²]. This interfacial perpendicular anisotropy is comparable to those reported for CoFeB/MgO systems [31,32], for the samples investigated in this work we cannot distinguish between the perpendicular anisotropy contribution from the IrMn interface and the Ru interface. However, given the large interfacial anisotropy present in the films it is likely that both interfaces contribute significantly.

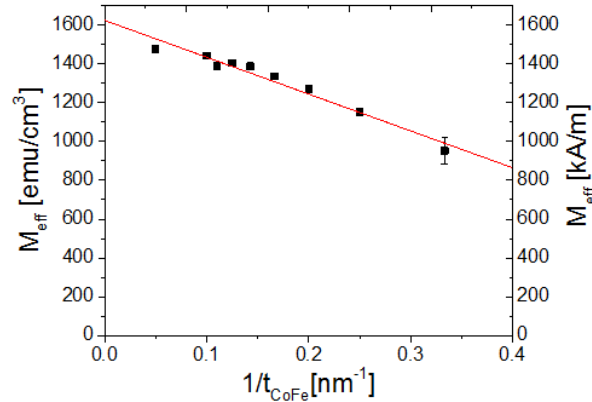


FIG. 2.3. Effective magnetization M_{eff} , determined using broadband ferromagnetic resonance data, as a function of the inverse CoFe film thickness t_{CoFe} . The red line is a linear fit of the experimental data.

It is worth noting that carrying out broadband ferromagnetic resonance measurements only for two in-plane orientations will limit the accuracy of extracting anisotropy field values. In particular, any misalignment of the exchange bias field direction of the sample relative to the applied field during measurement will result in inaccurate values for the exchange bias field H_{eb} and the uniaxial anisotropy field H_u . Furthermore, even if the external magnetic field is perfectly aligned with the exchange bias field direction but the easy axis of the uniaxial anisotropy does not coincide with the exchange bias direction, i.e. $\phi_u \neq 0$, the uniaxial anisotropy field will be systematically underestimated, as one is only sensitive to the component along the exchange bias field direction. We also find that the fitting parameters are highly correlated and thus the fit is not very sensitive to the value of the uniaxial anisotropy. With these limitations in mind, it is clear that a more exhaustive method is needed to extract precise values of the involved anisotropies. Ferromagnetic resonance measurements as a function of the in-plane angle of the applied magnetic field not only provide a way to extract the magnitude of the anisotropies, but also enable us to test the underlying assumption of our analysis, that the easy axis of the uniaxial anisotropy is aligned along the exchange bias direction.

B. In-plane angle dependent characterization

B.1 Ferromagnetic resonance

We have carried out ferromagnetic resonance measurements as a function of the in-plane angle of the applied field ϕ_H with respect to the exchange bias direction. As an example in Fig. 2.4 (a) the in-plane dependence of the resonance field measured at a microwave frequency of 20 GHz for a sample with a CoFe thickness of 6 nm is shown. In this figure a fit of the experimental data using the analytic model of Eq. (2.6) is shown as a green line. The full model based on Eq. (2.1),

and minimizing the free energy to obtain the equilibrium orientation of the magnetization, is shown as a red line. At first glance, both fits appear to reasonably describe the experimental data, as on the scale of Fig. 2.4(a) both models are difficult to distinguish. However, closer inspection of the residuals for both fits, as shown in Fig. 2.4(b), reveals that the use of Eq. (2.6) leads to systematic deviations that show a threefold symmetry. While there have been prior reports of a threefold anisotropy contribution in exchange bias systems [33], for the systems investigated in the current study, the threefold symmetry of the residuals is a result of the assumptions made to arrive at Eq.(2.6), in particular, the assumption that the magnetization is aligned with the direction of the applied field. In Fig. 2.4(c), the difference between the magnetization angle ϕ_0 and the applied field angle ϕ_H , calculated using the full model, is shown, revealing misalignments as large as 15 degrees. As can be seen in Fig. 2.4(b), using the full model results in residuals that do not show any clear angular dependence.

In order to verify that the threefold symmetry in the residuals is solely an artifact of the analytical model we have simulated the in-plane angular dependence of the resonance field using the full model and subsequently trying to fit this data using Eq. (2.6). These simulations also reveal that it is the presence of both the exchange bias field and the uniaxial anisotropy that lead to this apparent threefold symmetry. In the limiting case with no exchange bias field the residuals show a fourfold symmetry. We would also like to point out that while the uniaxial contribution to the resonance field H_u' in Eq. (2.6) is close to the value of the uniaxial anisotropy field H_u the two values are not identical. A more accurate determination of the latter value, for a system without exchange bias field, can be obtained by measuring the resonance field along the easy and hard direction and using Eq. (2.6) in reference [29]. In the limiting case with no uniaxial anisotropy but with an exchange bias field one can use Eq. (2.6) to fit the full model data with

reasonable accuracy, in this case the residuals again show a fourfold symmetry. A simulation and fit using Eq. (2.6) for the case of primary interest, where both an exchange bias field and a uniaxial anisotropy are present in the sample, is shown in Fig. 2.5. Here the exchange bias field was chosen

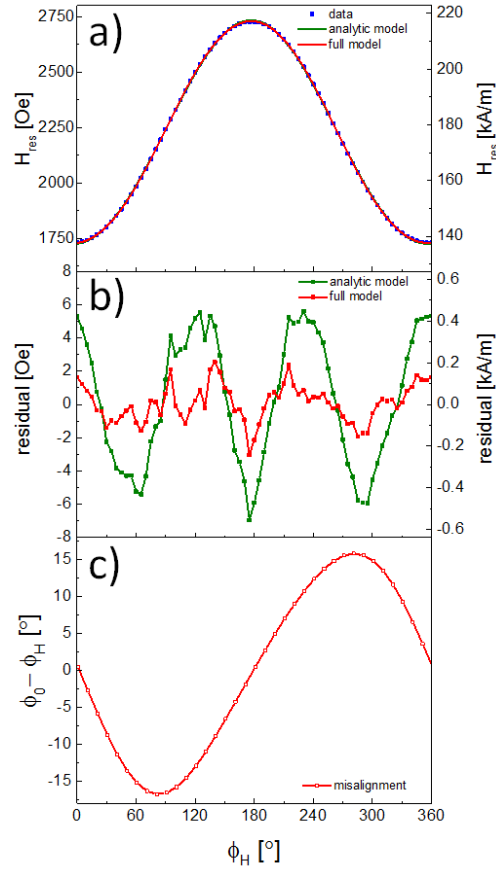


FIG. 2.4. Dependence on the in-plane angle of the applied field ϕ_H of (a) the resonance field H_{res} of a 6 nm CoFe exchange biased layer. The figure includes the experimental data (blue symbols), a fit using the analytic model (green line) and a fit using the full model (red line), (b) the residuals of the fit using the analytical model (green line & symbols) and the full model (red line & symbols) and (c) the misalignment of the in-plane angle of the magnetization ϕ_0 from the direction of the applied field ϕ_H calculated using the full model.

to be $H_{eb} = 500 [Oe]$ and the uniaxial anisotropy field was set to $H_u = 200 [Oe]$. By using a relatively large uniaxial anisotropy field the limitations of the simplified model become more obvious. This can be seen by comparing Fig. 2.5 (a) with Fig. 2.4 (a). Due to the strong uniaxial

anisotropy in Fig. 2.5 (a) a clear minimum exists for the resonance around $\phi_H = 180^\circ$ for the full model whereas for a smaller uniaxial anisotropy the deviations of the resonance field from a simple $\cos(\phi_H)$ dependence are more subtle, see Fig. 2.4 (a). As pointed out earlier the simplified model does not take into account the deviation of the equilibrium direction of the magnetization ϕ_0 from the direction of the applied field ϕ_H , which is shown in Fig. 2.5(c) and can reach 15 degrees,

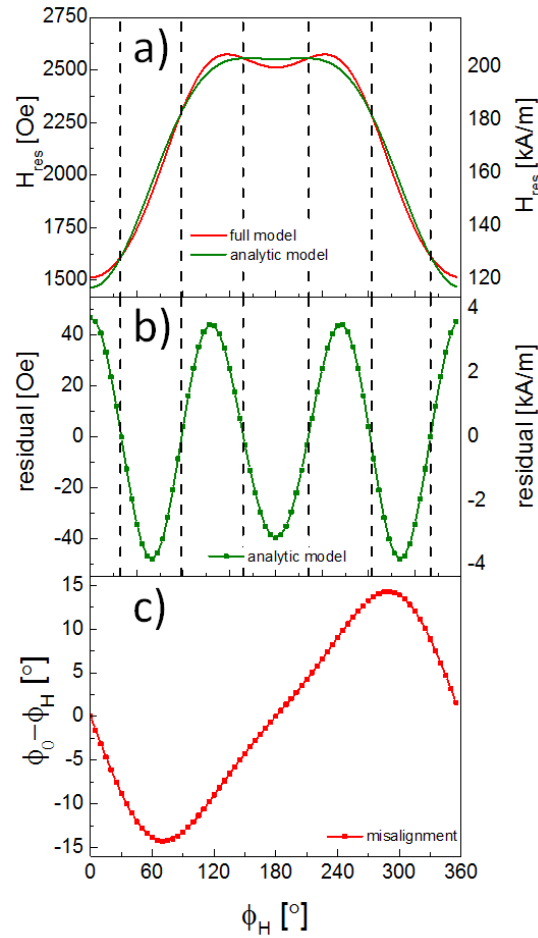


FIG. 2.5. Dependence on the in-plane angle of the applied field ϕ_H of (a) the resonance field H_{res} . The red line is the result of the full model for $H_{eb} = 500$ [Oe] and $H_u = 200$ [Oe], the green line is a fit of this data using Eq. (2.6), (b) the residuals of the fit and (c) the misalignment of the equilibrium direction of the magnetization ϕ_0 from the direction of the applied field ϕ_H .

similar to the experimental case depicted in Fig. 2.4. A fit of the analytical model of Eq. (2.6) to the simulated data of the full model can therefore not capture the observed angular dependence.

Because the fit attempts to minimize the sum of squares of the deviations this leads to an underestimation of the resonance field parallel to the exchange bias direction and an overestimation of the resonance field antiparallel to the exchange bias direction. As can be seen in Fig 2.5 (a) and 2.5 (b) over a full 360-degree rotation there will be six points for which the fit and the full simulation intersect (dashed lines), which explains that to first order the symmetry of the residual is threefold. However, as the full model did not contain a threefold contribution to the free energy this apparent threefold symmetry is an artifact of the assumptions made to derive Eq. (2.6), most notably the assumption that the magnetization is aligned with the external magnetic field. Thus while at first glance it may be tempting to add a threefold term to Eq. (2.6) similar to a Fourier series, our analysis shows that there is no physical significance to such a term and one should instead use the full model to arrive at meaningful parameters.

By fitting the full model to the in-plane angle dependence of the resonance field for all samples, we were able to extract the exchange bias field H_{eb} (see Fig 2.7) and the uniaxial anisotropy field H_u . Furthermore, the angle ϕ_H of the easy axis of the uniaxial anisotropy was treated as a free fitting parameter. However, within the error margins the easy axis of the uniaxial anisotropy is indeed parallel to the easy direction of the unidirectional anisotropy, which justifies our analysis of the broadband FMR data for which this was the assumption.

B2. Quasistatic magnetometry

We have also carried out in-plane angle dependent magnetization reversal measurements using the magneto-optical Kerr effect (MOKE) in longitudinal geometry. Measurements were carried out over a full 360-degree rotation and the linear and quadratic Kerr-effect contributions were separated using a procedure described in detail in reference [34]. The linear Kerr-effect signal was subsequently analyzed to determine the two coercive fields for the increasing and decreasing

field branch of the magnetization reversal. From this the shift of the reversal curves was determined as a function of the in-plane angle ϕ_H of the applied field. As can be seen in Fig 2.6 for a 6 nm thick CoFe film the angular dependence of the shift of the magnetization reversal curves is well described by a cosine dependence, i.e. $H_{eb}\cos(\phi_H)$, which is consistent with the unidirectional anisotropy in the films due to the exchange bias effect. While additional in-plane anisotropies in exchange bias films can lead to complex phase diagrams [10,11,34] and thereby to deviations from such a simple behavior, we find for the samples of this study that the additional in-plane uniaxial anisotropy is too small to have a significant influence on the angular dependence of the shift of the hysteresis curves. This is consistent with the results from the in-plane angle dependent ferromagnetic resonance measurements that also indicated that the uniaxial anisotropy field is small compared to the exchange bias field for all samples of this series.

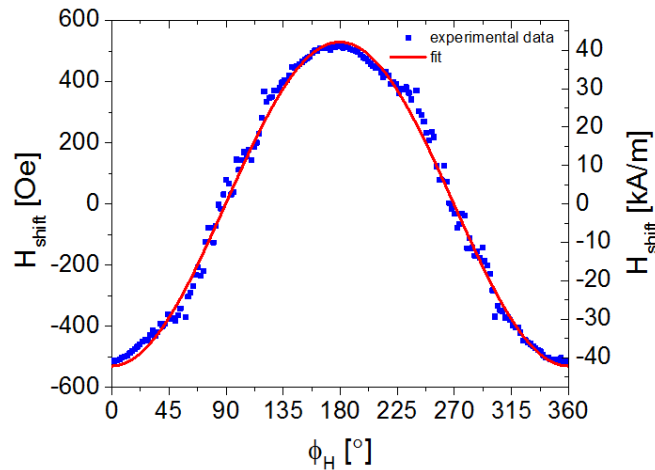


FIG. 2.6. Field shift H_{shift} of the magnetization reversal curves as a function of the in-plane angle ϕ_H of the applied field. Experimental data determined using the magneto-optic Kerr effect is shown as blue symbols, whereas the red line is a fit using $H_{shift}(\phi_H) = H_{eb}\cos(\phi_H)$.

In summary the exchange bias field that is extracted from the magnetization reversal curves agrees well with the value determined from ferromagnetic resonance data, see Fig. 2.7. Due to the interfacial nature of the exchange bias effect the exchange bias field is expected to

scale with the inverse of the thickness of the ferromagnetic layer [7,18,35], which is confirmed in Fig. 2.7. From the slope of this figure and the saturation magnetization determined earlier, one can determine the interface energy per unit area [7,36,37], also called interfacial exchange coupling, $\Delta\sigma = M_S \cdot t_{CoFe} \cdot H_{eb}$, which enables a comparison with other exchange bias systems. For the interfacial exchange coupling we obtain a value of $\Delta\sigma = 0.53 \pm 0.02$ [erg/cm²], which exceeds the values for all metallic antiferromagnets listed in Table 3 of reference [7] and is almost five times as big as the value reported in reference [38] for perpendicular CoFe/IrMn bilayers, which confirms the strong interfacial exchange coupling in our film series.

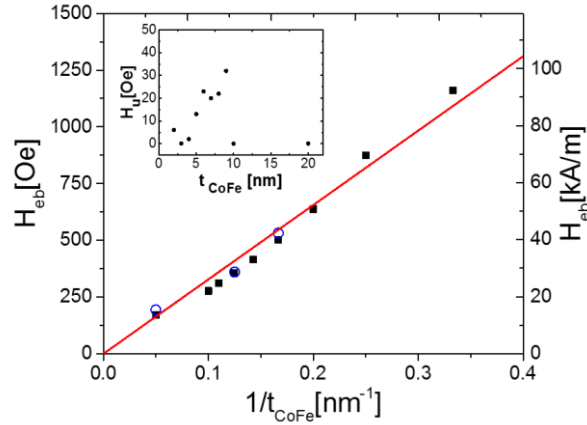


FIG. 2.7. Exchange bias field H_{eb} as a function of the inverse of the CoFe thickness t_{CoFe} as determined from ferromagnetic resonance data (black solid symbols) and MOKE data (blue open symbols). The red line shows a linear fit of the data. The inset shows the in-plane uniaxial anisotropy field as determined from ferromagnetic resonance data as a function of the CoFe thickness.

V. Magnetization relaxation

The linewidth of the ferromagnetic resonance contains information about the magnetization relaxation and inhomogeneities in the samples. Using Suhl's approach [39] one can obtain an approximate expression for the peak-to-peak linewidth contribution due to Gilbert-type damping [25,40-42]:

$$\Delta H_{Gilbert} \approx \frac{2}{\sqrt{3}} \frac{\alpha_{eff}}{\gamma} \frac{\omega}{\cos(\phi_0 - \phi_H)} \quad (2.7)$$

where α_{eff} is the effective Gilbert-type damping parameter and $\phi_0 - \phi_H$ is the misalignment between the magnetization and the external magnetic field. Under the assumption that the magnetization is perfectly aligned with the magnetic field and by including a zero frequency offset ΔH_0 that takes into account sample inhomogeneities one has for the peak-to-peak linewidth [40,41,43] :

$$\Delta H = \Delta H_0 + \frac{2}{\sqrt{3}} \frac{\alpha_{eff}}{\gamma} \omega \quad (2.8)$$

However, in thin films two-magnon scattering can contribute significantly to the ferromagnetic resonance linewidth measured with the magnetic field applied in the film plane. While the calculation of the two-magnon contribution ΔH_{2-mag} to the linewidth requires a quantitative model of the interfacial roughness, which is difficult to determine experimentally, under the assumptions for the roughness made by Arias and Mills one can obtain the following expression [44-46]:

$$\Delta H_{2-mag} = \Gamma(\omega) \arcsin \frac{\sqrt{\left(\frac{\omega_0}{2}\right)^2 + \omega^2} - \frac{\omega_0}{2}}{\sqrt{\left(\frac{\omega_0}{2}\right)^2 + \omega^2} + \frac{\omega_0}{2}} \quad (2.9)$$

with $\omega_0 = \gamma 4\pi M_{eff}$ and $\Gamma(\omega)$ is the strength of the two-magnon scattering, which depends on the details of the interfacial roughness. If the two-magnon is strictly interfacial the scattering strength should scale like the inverse ferromagnetic film thickness squared [9,17]. Furthermore, the scattering strength depends only weakly on the microwave frequency [44].

Thus one expects the ferromagnetic linewidth to be the sum of the contributions due to sample inhomogeneities, Gilbert-type damping and two-magnon scattering:

$$\Delta H = \Delta H_0 + \Delta H_{Gilbert} + \Delta H_{2-mag} \quad (2.10)$$

In Fig. 2.8(a) the ferromagnetic resonance linewidth for a 4 nm thick exchange biased CoFe film is shown. For the measurements that were carried out with the external magnetic field applied antiparallel to the exchange bias direction (red symbols) the frequency dependence of the linewidth is clearly nonlinear. The experimental data in this case can be fitted using the model for two-magnon scattering described by Eq. (2.9) with a frequency independent scattering strength (dashed red line in Fig. 2.8(a)). However, we note that the nonlinearity of the two-magnon scattering is weak and according to Eq. (2.9) for $\omega \ll \omega_0$ the two-magnon contribution is to a good approximation linear in frequency.

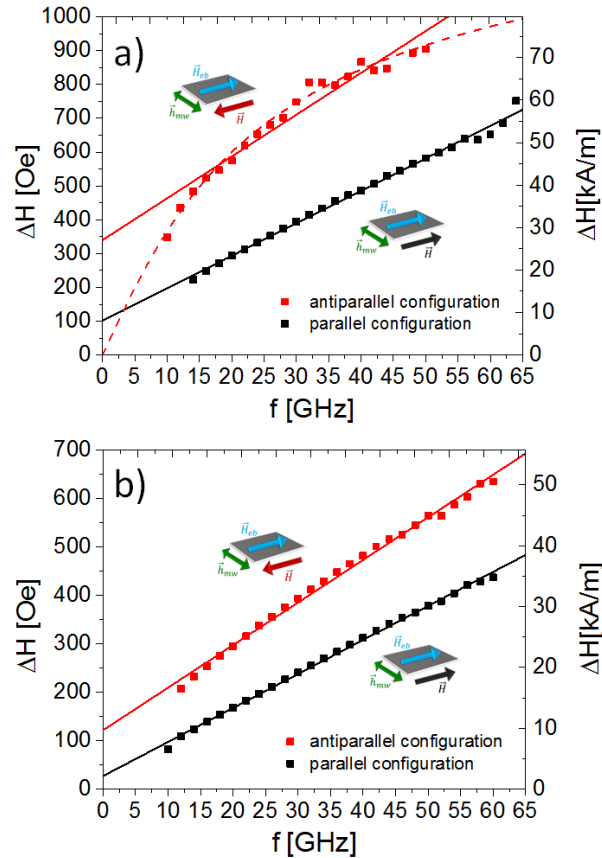


FIG. 2.8. Ferromagnetic resonance linewidth ΔH as a function of the microwave frequency f for a CoFe sample with a thickness of (a) $t_{\text{CoFe}} = 4$ [nm] and (b) $t_{\text{CoFe}} = 6$ [nm]. The black (red) symbols represent broadband FMR data measured with the field parallel (antiparallel) to the exchange bias direction. The solid lines show a fit of the data assuming Gilbert-type damping, Eq. (2.8), and the dashed line in (a) shows a fit of the data assuming two-magnon scattering as described by Eq. (2.9).

This property of the two-magnon scattering prevents fitting of the experimental data including all three contributions of the linewidth, as the fitting parameters in this case are highly correlated and not unique. Because the two-magnon scattering scales with t_{CoFe}^{-2} its relative contribution to the overall ferromagnetic resonance linewidth decreases quickly with increasing film thickness, as can be seen in Fig. 2.8(b). In this figure the ferromagnetic resonance linewidth for a 6 nm thick exchange biased CoFe film is shown as a function of the microwave frequency. In this case the nonlinearity of the frequency dependence of the linewidth caused by the two-magnon scattering, while still noticeable, is not very pronounced. Because of the difficulties to separate the Gilbert-type damping contribution and the two-magnon scattering contribution to the linewidth we therefore analyze the data by neglecting the nonlinearity of the two-magnon contribution to the linewidth and instead fitting the data using only the zero frequency offset ΔH_0 due to inhomogeneities and an effective Gilbert-type damping α_{eff} , which in this approach also includes the two-magnon contribution.

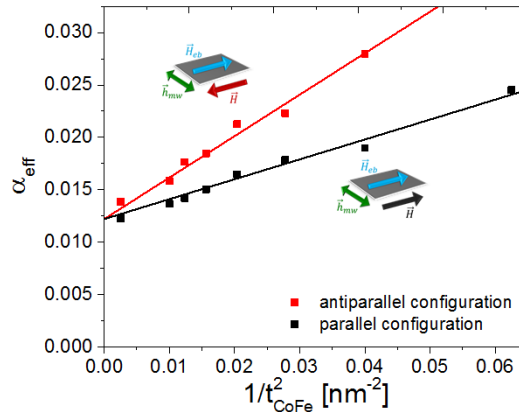


FIG. 2.9. Effective Gilbert-type damping parameter α_{eff} as a function of the square of the inverse CoFe thickness t_{CoFe} . The black (red) symbols represent damping parameters determined from broadband FMR data measured with the field parallel (antiparallel) to the exchange bias direction. The solid lines show linear fits of the data.

Accordingly, as shown in Fig. 2.9, the effective damping parameter scales approximately with the inverse ferromagnetic film thickness squared, indicating that two-magnon scattering is

the dominant relaxation mechanism for the thinnest films of the series. This figure also shows clearly that the relaxation in these exchange biased films is anisotropic and in particular is significantly larger when the magnetic field is applied antiparallel to the exchange bias direction compared to the parallel case. This suggests that the relaxation is unidirectional in nature as had been reported previously for NiFe/FeMn exchange bias structures [21].

To further investigate the unidirectional nature of the relaxation we have carried out in-plane angle dependent measurements of the ferromagnetic resonance linewidth at a fixed frequency, as shown in Fig. 2.10. Because the scattering strength of two-magnon scattering in thin films is determined by the perturbations at the interface it will reflect the in-plane angular dependence of these perturbations [42,44,47-51]. In the case of exchange bias systems one therefore expects the linewidth to show a unidirectional anisotropy as a function of the magnetization direction ϕ_0 , i.e.:

$$\Delta H(\phi_H) = \Delta H_{min} + \frac{\Delta H_{eb}}{2}(1 - \cos \phi_0) \quad (2.11)$$

Here ΔH_{min} represents the minimal linewidth, measured parallel to the exchange bias direction. This term includes the Gilbert-type damping and isotropic contributions to the linewidth at the measurement frequency. The magnitude of the unidirectional contribution to the linewidth is characterized by the parameter ΔH_{eb} . Through the magnetization direction ϕ_0 the linewidth depends on the direction of the external magnetic field ϕ_H , which is varied in the experiment. If one assumes that the magnetization is aligned with the external magnetic field Eq. (2.11) results in a simple cosine dependence of the linewidth with respect to the applied field direction. However, as discussed earlier, for the samples of the current study this assumption is not a good approximation, given the large misalignments we observe (compare Fig. 2.4 (c)).

Correspondingly an attempt to fit the experimental data with a simple cosine dependence results

in a systematic two-fold symmetry of the residuals (Fig. 2.10 (b)), which could lead to the erroneous introduction of an additional relaxation mechanism with this symmetry. In contrast using the full model discussed earlier, which minimized the free energy of the system to obtain the magnetization direction, results in an excellent description of the experimental data using only two fitting parameters.

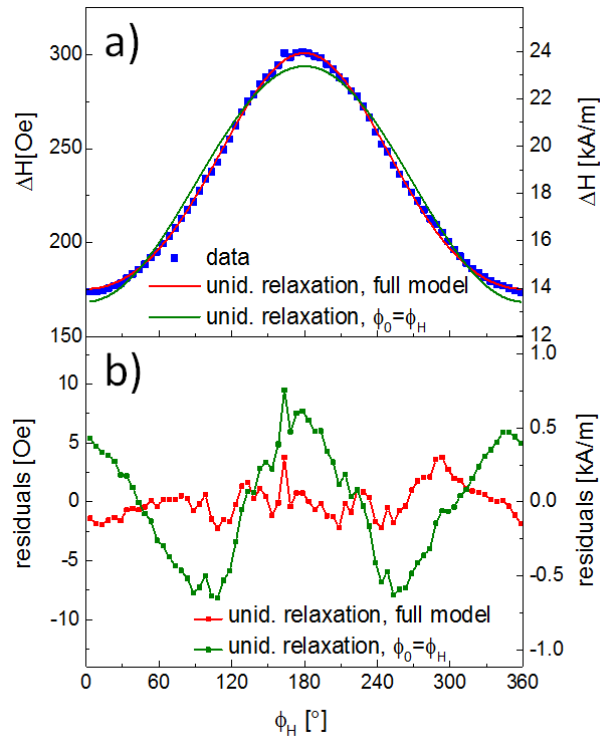


FIG. 2.10. (a) Peak-to-peak ferromagnetic resonance linewidth ΔH as a function of the in-plane angle ϕ_H of the applied field measured for a 6 nm thick exchange biased CoFe film at a microwave frequency of $f = 20$ [GHz]. Experimental data is shown as blue symbols, the red and green lines represent fits using a unidirectional relaxation described by Eq. (2.11) using the full model and assuming $\phi_0 = \phi_H$ respectively. (b) Residuals of the two different fits.

In Fig. 2.11 a) the magnitude of the unidirectional contribution to the linewidth ΔH_{eb} determined for all samples by fitting the experimental data using Eq. (2.11) is shown as a function of the inverse square of the CoFe thickness t_{CoFe} . If the unidirectional linewidth contribution was solely caused by a strictly interfacial two-magnon scattering one would expect

it to be proportional to $1/t_{\text{CoFe}}^2$. This is because in this case the two-magnon scattering scales with the square of the scattering potential, which is proportional to the inverse of the ferromagnetic film thickness [9,17,18,21]. However, the blue fit curve in Fig. 2.11 (a), which uses this relationship, results in a poor description of the data. In Fig. 2.11 (b) we have therefore included an additional unidirectional contribution to the linewidth that scales with the inverse film thickness to fit the data. As can be seen in the figure this results in a better description of the data. The fit also indicates that for films thinner than approximately 5 nm the two magnon contribution is stronger than the contribution that scales with the inverse CoFe film thickness, whereas for thicker films the situation is reversed. Besides its scaling with the inverse square of the CoFe film thickness, the two-magnon scattering contribution is also expected to lead to a non-linear frequency dependence of the linewidth which as previously discussed was observed to be significantly stronger for thinner films (Fig. 2.8). We therefore conclude that the samples investigated in this study show strong evidence for the presence of a unidirectional contribution to the relaxation in exchange biased films that is not caused by strictly interfacial two-magnon scattering.

While the possibility of unidirectional relaxation mechanisms involving conduction electrons at the interface with the antiferromagnet has been discussed in reference [21], more theoretical work is needed to obtain a quantitative description.

VI. Summary

We have carried out broadband ferromagnetic resonance characterization of a series of IrMn/CoFe exchange biased bilayers. In addition to a strong exchange bias effect our results show a significant reduction of the effective magnetization of the CoFe films with decreasing film thickness, caused by the presence of a strong interfacial perpendicular anisotropy. For in-

plane angle dependent ferromagnetic resonance measurements we have shown that an analytical model that is commonly used to describe this kind of data has limitations regarding the extraction of anisotropies and introduces artifacts that could be misinterpreted as an additional threefold anisotropy. However, using the full model, which properly minimizes the free energy

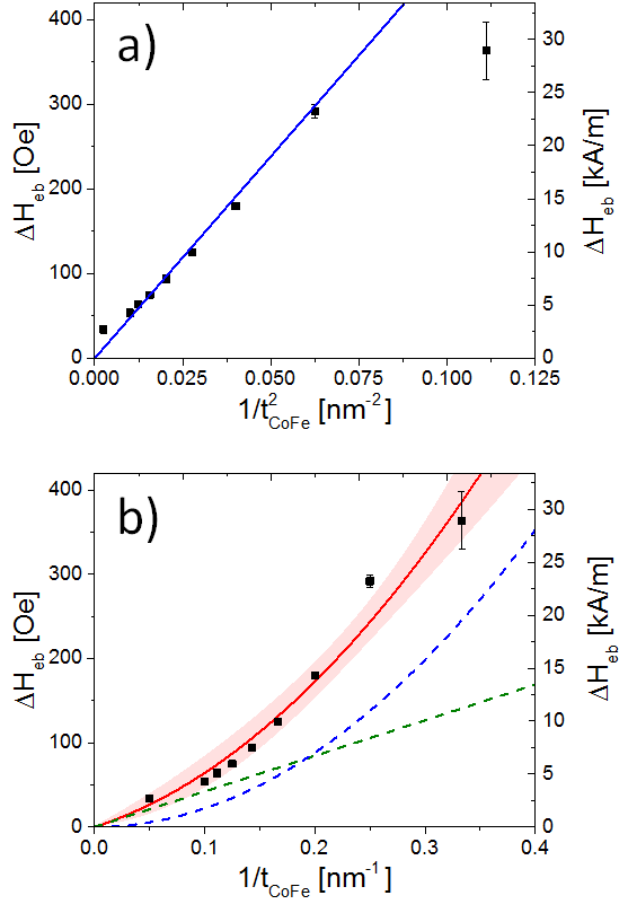


FIG. 2.11. Unidirectional linewidth contribution ΔH_{eb} determined from in-plane angle dependent FMR measurements. In (a) this contribution is plotted as a function of $1/t_{CoFe}^2$, the blue line is a linear fit of the data with a vanishing unidirectional linewidth contribution for the bulk. In part (b) the same data is shown as a function of the inverse CoFe thickness t_{CoFe} . The red line is a fit including a contribution linear (dashed green line) and quadratic (dashed blue line) in the inverse film thickness. The red shaded area indicates the 95% confidence bands of the fit.

of the system, enables a precise determination of the exchange bias field and a small in-plane uniaxial anisotropy that is also present in these bilayers. The results of our ferromagnetic resonance characterization are in good agreement with results obtained using quasistatic

magnetization reversal curves. The interface energy of the exchange bias effect in our sample series exceeds values previously reported for metallic antiferromagnets.

Our frequency and in-plane angle dependent measurements of the ferromagnetic resonance linewidth indicate a strong unidirectional contribution to the relaxation in the films. Part of this unidirectional relaxation can be attributed to two-magnon scattering at the CoFe interface to the antiferromagnet. However, the thickness dependence of the unidirectional linewidth contribution extracted from in-plane angle dependent measurements strongly suggests the presence of an additional unidirectional relaxation mechanism, i.e. a unidirectional relaxation not caused by strictly interfacial two-magnon scattering.

VII.Acknowledgements

We would like to acknowledge support by NSF-CAREER Award # 0952929 and by NSF-CAREER Award # 1452670.

VIII. References

- [1] W.H. Meiklejohn and C.P. Bean, New Magnetic Anisotropy, *Physical Review* **102**, 1413 (1956), <http://link.aps.org/doi/10.1103/PhysRev.102.1413>.
- [2] W.H. Meiklejohn and C.P. Bean, New Magnetic Anisotropy, *Physical Review* **105**, 904 (1957), <http://link.aps.org/doi/10.1103/PhysRev.105.904>.
- [3] S. Gider, B.-U. Runge, A.C. Marley, and S.S.P. Parkin, The Magnetic Stability of Spin-Dependent Tunneling Devices, *Science* **281**, 797 (1998), [10.1126/science.281.5378.797](https://doi.org/10.1126/science.281.5378.797).
- [4] A.V. Khvalkovskiy, D. Apalkov, S. Watts, R. Chepulskii, R.S. Beach, A. Ong, X. Tang, A. Driskill-Smith, W.H. Butler, P.B. Visscher, D. Lottis, E. Chen, V. Nikitin, and M. Krounbi, Basic principles of STT-MRAM cell operation in memory arrays, *Journal of Physics D: Applied Physics* **46**, 074001 (2013), <http://stacks.iop.org/0022-3727/46/i=7/a=074001>.
- [5] E. Chen, D. Apalkov, A. Driskill-Smith, A. Khvalkovskiy, D. Lottis, K. Moon, V. Nikitin, A. Ong, X. Tang, S. Watts, R. Kawakami, M. Krounbi, S.A. Wolf, S.J. Poon, J.W. Lu, A.W. Ghosh, M. Stan, W. Butler, T. Mewes, S. Gupta, C.K.A. Mewes, P.B. Visscher, and R.A. Lukaszew, Progress and Prospects of Spin Transfer Torque Random Access Memory, *IEEE Transactions on Magnetics* **48**, 3025 (2012), [10.1109/TMAG.2012.2198451](https://doi.org/10.1109/TMAG.2012.2198451).
- [6] R.L. Stamps, Mechanisms for exchange bias, *Journal of Physics D: Applied Physics* **33**, R247 (2000), <http://stacks.iop.org/0022-3727/33/i=23/a=201>.
- [7] J. Nogués and I.K. Schuller, Exchange bias, *Journal of Magnetism and Magnetic Materials* **192**, 203 (1999), [http://dx.doi.org/10.1016/S0304-8853\(98\)00266-2](http://dx.doi.org/10.1016/S0304-8853(98)00266-2).
- [8] J.C. Scott, Ferromagnetic resonance studies in the bilayer system Ni_{0.80}Fe_{0.20}/Mn_{0.50}Fe_{0.50}: Exchange anisotropy, *Journal of Applied Physics* **57**, 3681 (1985), doi:<http://dx.doi.org/10.1063/1.334987>.
- [9] R.D. McMichael, M.D. Stiles, P.J. Chen, and W.F. Egelhoff, Ferromagnetic resonance linewidth in thin films coupled to NiO, *Journal of Applied Physics* **83**, 7037 (1998), doi:<http://dx.doi.org/10.1063/1.367725>.
- [10] T. Mewes, H. Nembach, M. Rickart, S.O. Demokritov, J. Fassbender, and B. Hillebrands, Angular dependence and phase diagrams of exchange-coupled epitaxial Ni₈₁Fe₁₉/Fe₅₀Mn₅₀ (001) bilayers, *Physical Review B* **65**, 224423 (2002), <http://link.aps.org/doi/10.1103/PhysRevB.65.224423>.
- [11] T. Mewes, H. Nembach, J. Fassbender, B. Hillebrands, J.-V. Kim, and R.L. Stamps, Phase diagrams and energy barriers of exchange-biased bilayers with additional anisotropies in the ferromagnet, *Physical Review B* **67**, 104422 (2003), <http://link.aps.org/doi/10.1103/PhysRevB.67.104422>.

- [12] J. Fassbender, S. Poppe, T. Mewes, A. Mougin, B. Hillebrands, D. Engel, M. Jung, A. Ehresmann, H. Schmoranzer, G. Faini, K.J. Kirk, and J.N. Chapman, Magnetization Reversal of Exchange Bias Double Layers Magnetically Patterned by Ion Irradiation, *physica status solidi (a)* **189**, 439 (2002), [10.1002/1521-396X\(200202\)189:2<439::AID-PSSA439>3.0.CO;2-4](https://doi.org/10.1002/1521-396X(200202)189:2<439::AID-PSSA439>3.0.CO;2-4).
- [13] H.S. Cho, C. Hou, M. Sun, and H. Fujiwara, Characteristics of 360° -domain walls observed by magnetic force microscope in exchange-biased NiFe films, *Journal of Applied Physics* **85**, 5160 (1999), [doi:http://dx.doi.org/10.1063/1.369110](https://doi.org/10.1063/1.369110).
- [14] J. McCord, R. Schäfer, R. Mattheis, and K.-U. Barholz, Kerr observations of asymmetric magnetization reversal processes in CoFe/IrMn bilayer systems, *Journal of Applied Physics* **93**, 5491 (2003), [doi:http://dx.doi.org/10.1063/1.1562732](https://doi.org/10.1063/1.1562732).
- [15] J. McCord and S. Mangin, Separation of low- and high-temperature contributions to the exchange bias in $\text{Ni}_{81}\text{Fe}_{19}$ -NiO thin films, *Physical Review B* **88**, 014416 (2013), <http://link.aps.org/doi/10.1103/PhysRevB.88.014416>.
- [16] W. Stoecklein, S.S.P. Parkin, and J.C. Scott, Ferromagnetic resonance studies of exchange-biased Permalloy thin films, *Physical Review B* **38**, 6847 (1988), <http://link.aps.org/doi/10.1103/PhysRevB.38.6847>.
- [17] S.M. Rezende, A. Azevedo, M.A. Lucena, and F.M. de Aguiar, Anomalous spin-wave damping in exchange-biased films, *Physical Review B* **63**, 214418 (2001), <http://link.aps.org/doi/10.1103/PhysRevB.63.214418>.
- [18] S.M. Rezende, M.A. Lucena, A. Azevedo, F.M. de Aguiar, J.R. Fermin, and S.S.P. Parkin, Exchange anisotropy and spin-wave damping in CoFe/IrMn bilayers, *Journal of Applied Physics* **93**, 7717 (2003), [doi:http://dx.doi.org/10.1063/1.1543126](https://doi.org/10.1063/1.1543126).
- [19] S. Riedling, M. Bauer, C. Mathieu, B. Hillebrands, R. Jungblut, J. Kohlhepp, and A. Reinders, In-plane anomalies of the exchange bias field in $\text{Ni}_{80}\text{Fe}_{20}/\text{Fe}_{50}\text{Mn}_{50}$ bilayers on Cu(110), *Journal of Applied Physics* **85**, 6648 (1999), [doi:http://dx.doi.org/10.1063/1.370174](https://doi.org/10.1063/1.370174).
- [20] D.L. Mills and S.M. Rezende, in *Spin Dynamics in Confined Magnetic Structures II*, edited by B. Hillebrands, and K. Ounadjela (Springer Berlin Heidelberg, Berlin, Heidelberg, 2003), pp. 27.
- [21] T. Mewes, R.L. Stamps, H. Lee, E. Edwards, M. Bradford, C.K.A. Mewes, Z. Tadisina, and S. Gupta, Unidirectional Magnetization Relaxation in Exchange-Biased Films, *Magnetics Letters*, *IEEE* **1**, 3500204 (2010), [10.1109/LMAG.2010.2055552](https://doi.org/10.1109/LMAG.2010.2055552).
- [22] M. Ali, C.H. Marrows, M. Al-Jawad, B.J. Hickey, A. Misra, U. Nowak, and K.D. Usadel, Antiferromagnetic layer thickness dependence of the IrMn/Co exchange-bias system, *Physical Review B* **68**, 214420 (2003), <http://link.aps.org/doi/10.1103/PhysRevB.68.214420>.

[23] C.J. Oates, F.Y. Ogrin, S.L. Lee, P.C. Riedi, G.M. Smith, and T. Thomson, High field ferromagnetic resonance measurements of the anisotropy field of longitudinal recording thin-film media, *Journal of Applied Physics* **91**, 1417 (2002), doi:http://dx.doi.org/10.1063/1.1428804.

[24] N. Pachauri, B. Khodadadi, M. Althammer, A.V. Singh, B. Loukya, R. Datta, M. Iliev, L. Bezmaternykh, I. Gudim, T. Mewes, and A. Gupta, Study of structural and ferromagnetic resonance properties of spinel lithium ferrite (LiFe₅O₈) single crystals, *Journal of Applied Physics* **117**, 233907 (2015), doi:http://dx.doi.org/10.1063/1.4922778.

[25] K.A.M. Claudia and M. Tim, in *Handbook of Nanomagnetism* (Pan Stanford, 2015), pp. 71.

[26] P.G. Barreto, M.A. Sousa, F. Pelegrini, W. Alayo, F.J. Litterst, and E. Baggio-Saitovitch, Ferromagnetic resonance study of the misalignment between anisotropy axes in exchange-biased NiFe/FeMn/Co trilayers, *Applied Physics Letters* **104**, 202403 (2014), doi:http://dx.doi.org/10.1063/1.4875929.

[27] H. Xi, K.R. Mountfield, and R.M. White, Ferromagnetic resonance studies of exchange biasing in Ni₈₁Fe₁₉/Pt₁₀Mn₉₀ bilayers, *Journal of Applied Physics* **87**, 4367 (2000), doi:http://dx.doi.org/10.1063/1.373080.

[28] This can be seen for example by noting that in the limit of vanishing exchange bias field, i.e.

$H_{eb} = 0$ equation (2.5) along the easy axis of the uniaxial anisotropy ($\phi_H = 0^\circ$) simplifies to:

$$f = \frac{\gamma}{2\pi} \sqrt{[4\pi M_{eff} + H_u + H_{res,0}] \cdot [H_u + H_{res,0}]} \quad (f1)$$

Whereas along the hard axis of the uniaxial anisotropy ($\phi_H = 90^\circ$) using equation (2.4) one has:

$$f = \frac{\gamma}{2\pi} \sqrt{[4\pi M_{eff} + H_{res,90}] \cdot [-H_u + H_{res,90}]} \quad (f2)$$

From measurements of the resonance field at the same frequency f along the easy ($H_{res,0}$) and hard axis ($H_{res,90}$) one can therefore extract the uniaxial anisotropy field as follows:

$$H_u = \frac{-H_1 + \sqrt{H_1^2 - 4H_2}}{2} \quad (f3)$$

with $H_1 = 2(H_{res,0} + 4\pi M_{eff}) + H_{res,90}$ and $H_2 = H_{res,0} \cdot (H_{res,0} + 4\pi M_{eff}) - H_{res,90} \cdot (H_{res,90} + 4\pi M_{eff})$. Note that this result is similar to reference [29], where an expression for H_u was derived assuming $H_u \ll 4\pi M_{eff}$. Whereas for equation (2.6) in the limit of vanishing

exchange bias field one has simply: $H'_u = \frac{H_{res,90} - H_{res,0}}{2}$ (f4)

[29] G.N. Kakazei, P.E. Wigen, K.Y. Guslienko, R.W. Chantrell, N.A. Lesnik, V. Metlushko, H. Shima, K. Fukamichi, Y. Otani, and V. Novosad, In-plane and out-of-plane uniaxial anisotropies in rectangular arrays of circular dots studied by ferromagnetic resonance, *Journal of Applied Physics* **93**, 8418 (2003), doi:http://dx.doi.org/10.1063/1.1556978.

- [30] J.M. Shaw, H.T. Nembach, T.J. Silva, and C.T. Boone, Precise determination of the spectroscopic g-factor by use of broadband ferromagnetic resonance spectroscopy), *Journal of Applied Physics* **114**, 243906 (2013), doi:<http://dx.doi.org/10.1063/1.4852415>.
- [31] D.C. Worledge, G. Hu, D.W. Abraham, J.Z. Sun, P.L. Trouilloud, J. Nowak, S. Brown, M.C. Gaidis, E.J. O'Sullivan, and R.P. Robertazzi, Spin torque switching of perpendicular Ta|CoFeB|MgO-based magnetic tunnel junctions, *Applied Physics Letters* **98**, 022501 (2011), doi:<http://dx.doi.org/10.1063/1.3536482>.
- [32] J. Sinha, M. Hayashi, A.J. Kellock, S. Fukami, M. Yamanouchi, H. Sato, S. Ikeda, S. Mitani, S.-h. Yang, S.S.P. Parkin, and H. Ohno, Enhanced interface perpendicular magnetic anisotropy in Ta|CoFeB|MgO using nitrogen doped Ta underlayers, *Applied Physics Letters* **102**, 242405 (2013), doi:<http://dx.doi.org/10.1063/1.4811269>.
- [33] I.N. Krivorotov, C. Leighton, J. Nogués, I.K. Schuller, and E.D. Dahlberg, Relation between exchange anisotropy and magnetization reversal asymmetry in Fe/MnF₂ bilayers, *Physical Review B* **65**, 100402 (2002), <http://link.aps.org/doi/10.1103/PhysRevB.65.100402>.
- [34] T. Mewes, H. Nembach, M. Rickart, and B. Hillebrands, Separation of the first- and second-order contributions in magneto-optic Kerr effect magnetometry of epitaxial FeMn/NiFe bilayers, *Journal of Applied Physics* **95**, 5324 (2004), doi:<http://dx.doi.org/10.1063/1.1697640>.
- [35] Y.J. Tang, B. Roos, T. Mewes, S.O. Demokritov, B. Hillebrands, and Y.J. Wang, Enhanced coercivity of exchange-bias Fe/MnPd bilayers, *Applied Physics Letters* **75**, 707 (1999), doi:<http://dx.doi.org/10.1063/1.124489>.
- [36] A.E. Berkowitz and K. Takano, Exchange anisotropy — a review, *Journal of Magnetism and Magnetic Materials* **200**, 552 (1999), [http://dx.doi.org/10.1016/S0304-8853\(99\)00453-9](http://dx.doi.org/10.1016/S0304-8853(99)00453-9).
- [37] A.P. Malozemoff, Random-field model of exchange anisotropy at rough ferromagnetic-antiferromagnetic interfaces, *Physical Review B* **35**, 3679 (1987), <http://link.aps.org/doi/10.1103/PhysRevB.35.3679>.
- [38] J.Y. Chen, N. Thiyagarajah, H.J. Xu, and J.M.D. Coey, Perpendicular exchange bias effect in sputter-deposited CoFe/IrMn bilayers, *Applied Physics Letters* **104**, 152405 (2014), doi:<http://dx.doi.org/10.1063/1.4871711>.
- [39] H. Suhl, Ferromagnetic Resonance in Nickel Ferrite Between One and Two Kilomegacycles, *Physical Review* **97**, 555 (1955), <http://link.aps.org/doi/10.1103/PhysRev.97.555.2>.
- [40] B. Heinrich, J.F. Cochran, and R. Hasegawa, FMR linebroadening in metals due to two-magnon scattering, *Journal of Applied Physics* **57**, 3690 (1985), doi:<http://dx.doi.org/10.1063/1.334991>.

- [41] Z. Celinski and B. Heinrich, Ferromagnetic resonance linewidth of Fe ultrathin films grown on a bcc Cu substrate, *Journal of Applied Physics* **70**, 5935 (1991), doi:<http://dx.doi.org/10.1063/1.350110>.
- [42] Y.V. Goryunov, N.N. Garif'yanov, G.G. Khaliullin, I.A. Garifullin, L.R. Tagirov, F. Schreiber, T. Mühge, and H. Zabel, Magnetic anisotropies of sputtered Fe films on MgO substrates, *Physical Review B* **52**, 13450 (1995), <http://link.aps.org/doi/10.1103/PhysRevB.52.13450>.
- [43] T.D. Rossing, Resonance Linewidth and Anisotropy Variation in Thin Films, *Journal of Applied Physics* **34**, 995 (1963), doi:<http://dx.doi.org/10.1063/1.1729582>.
- [44] R. Arias and D.L. Mills, Extrinsic contributions to the ferromagnetic resonance response of ultrathin films, *Physical Review B* **60**, 7395 (1999), <http://link.aps.org/doi/10.1103/PhysRevB.60.7395>.
- [45] R. Arias and D.L. Mills, Extrinsic contributions to the ferromagnetic resonance response of ultrathin films, *Journal of Applied Physics* **87**, 5455 (2000), doi:<http://dx.doi.org/10.1063/1.373370>.
- [46] D.L. Mills and R. Arias, The damping of spin motions in ultrathin films: Is the Landau–Lifschitz–Gilbert phenomenology applicable?, *Physica B: Condensed Matter* **384**, 147 (2006), <http://dx.doi.org/10.1016/j.physb.2006.05.209>.
- [47] J. Lindner, K. Lenz, E. Kosubek, K. Baberschke, D. Spoddig, R. Meckenstock, J. Pelzl, Z. Frait, and D.L. Mills, Non-Gilbert-type damping of the magnetic relaxation in ultrathin ferromagnets: Importance of magnon-magnon scattering, *Physical Review B* **68**, 060102 (2003), <http://link.aps.org/doi/10.1103/PhysRevB.68.060102>.
- [48] G. Woltersdorf and B. Heinrich, Two-magnon scattering in a self-assembled nanoscale network of misfit dislocations, *Physical Review B* **69**, 184417 (2004), <http://link.aps.org/doi/10.1103/PhysRevB.69.184417>.
- [49] K. Lenz, H. Wende, W. Kuch, K. Baberschke, K. Nagy, and A. Jánossy, Two-magnon scattering and viscous Gilbert damping in ultrathin ferromagnets, *Physical Review B* **73**, 144424 (2006), <http://link.aps.org/doi/10.1103/PhysRevB.73.144424>.
- [50] I. Barsukov, P. Landeros, R. Meckenstock, J. Lindner, D. Spoddig, Z.-A. Li, B. Krumme, H. Wende, D.L. Mills, and M. Farle, Tuning magnetic relaxation by oblique deposition, *Physical Review B* **85**, 014420 (2012), <http://link.aps.org/doi/10.1103/PhysRevB.85.014420>.
- [51] H. Kurebayashi, T.D. Skinner, K. Khazen, K. Olejník, D. Fang, C. Ciccarelli, R.P. Campion, B.L. Gallagher, L. Fleet, A. Hirohata, and A.J. Ferguson, Uniaxial anisotropy of two-magnon scattering in an ultrathin epitaxial Fe layer on GaAs, *Applied Physics Letters* **102**, 062415 (2013), doi:<http://dx.doi.org/10.1063/1.4792269>.

3. FERROMAGNETIC RESONANCE STUDY OF INTERFACIAL PERPENDICULAR ANISOTROPY IN $\text{Ni}_{0.8}\text{Fe}_{0.2}/\text{Ru}$ AND $\text{Ni}_{0.8}\text{Fe}_{0.2}/\text{SiO}_2$ INTERFACES

Jamileh Beik Mohammadi^{1,2}, Gary Mankey^{1,2}, Claudia K. A. Mewes^{1,2}, Tim Mewes^{1,2}

1: Center for Materials for Information Technology, University of Alabama, Tuscaloosa, Alabama 35487

2: Department of Physics and Astronomy, University of Alabama, Tuscaloosa, Alabama 35487

We report on a strong perpendicular magnetic anisotropy in $\text{Ni}_{0.8}\text{Fe}_{0.2}$ thin films that originates from the interfaces with adjacent Ru and SiO_2 layers. Moreover, magnetic relaxation analyses confirm that the Gilbert damping in these films are comparatively smaller than the $\text{SiO}_2/\text{Ni}_{0.8}\text{Fe}_{0.2}/\text{Ru}$ films and $\text{Ru}/\text{Ni}_{0.8}\text{Fe}_{0.2}/\text{Ru}$ films.

I. Introduction

Investigating perpendicular anisotropy in different structures and materials is of significant importance as it is a key parameter in many applications such as magnetic tunnel junctions (MTJs), spin transfer torque magnetic random access memory (STT-MRAM), and read

heads for magnetic recording [1]. Proximity effects from capping or buffer layers can create a strong perpendicular anisotropy in the adjacent ferromagnetic layer [2]. This interfacial anisotropy has been a point of interest for many researchers [1,3-5]. One reason for this is that the origin of the interfacial perpendicular anisotropy remains ambiguous [1] and can be affected by electronic effects, morphology, or the strain effects at the interface. However, it is known that the hybridization of atomic orbitals plays an important role in creating a strong interfacial perpendicular anisotropy [6]. Normal metals such as Ru [7] are known for creating perpendicular anisotropy in the adjacent ferromagnetic layers [1]. Some oxides such as Al₂O₃ [8] and MgO are also known to create perpendicular anisotropy in thin ferromagnetic layers like CoFeB [1,9-11], CoFeAl [12], Cobalt [5,13], Fe [14], and Ni_{0.8}Fe_{0.2} [15,16] to our knowledge the effect of SiO₂ on creating interfacial anisotropy in adjacent ferromagnetic layer such as Ni_{0.8}Fe_{0.2} has not been reported.

Here we have deposited three different sets of samples and have studied the interfacial perpendicular anisotropy in Ni_{0.8}Fe_{0.2}/Ru and Ni_{0.8}Fe_{0.2}/SiO₂ interfaces using broadband ferromagnetic resonance (FMR) measurements.

II.Experimental procedure

In order to examine the effect of SiO₂ and Ru on the interfacial perpendicular anisotropy and the magnetization dynamics of Ni_{0.8}Fe_{0.2} thin films, we have deposited three sets of samples using DC and RF magnetron sputtering at room temperature. The substrates are Si <100> wafers with a thin layer of native oxide on them ($t_{SiO_2} \approx 20 \text{ nm}$). The base pressure before deposition was $2 \times 10^{-8} \text{ Torr}$. Argon pressure during deposition is maintained at 4 mTorr using a closed-loop feedback system with an adjustable conductance valve and constant argon flow of 20 sccm. The same deposition conditions were maintained for the fabrication of

Si/SiO₂/Ni_{0.8}Fe_{0.2}(x)/Ru(4nm), Si/SiO₂/Ni_{0.8}Fe_{0.2}(x)/SiO₂, and Si/SiO₂/Ru(4nm)/Ni_{0.8}Fe_{0.2}(x)/Ru(4nm). The thickness of the Ni_{0.8}Fe_{0.2} layer, x, was varied between 2nm and 12nm by changing the deposition time. X-Ray reflectivity measurements were used to calibrate the deposition rate of the Ni_{0.8}Fe_{0.2} layer which was 0.7 Å/s.

III. Results and discussion

Ferromagnetic resonance (FMR) is a powerful tool to investigate the interfacial anisotropy in thin ferromagnetic films. In this work, broadband FMR is utilized to study magnetic properties of samples described in section II a frequency ranges of 4GHz-60GHz. By fitting the raw FMR data to the derivative of a Lorentzian, the precise value of the resonance field (H_{res}) and linewidth (ΔH) is determined at each frequency. The field dependence of the resonance frequency is then fitted to the Kittel equation (Equation (3.1)):

$$f = \gamma' \sqrt{H_{res}(H_{res} + 4\pi M_{eff})} \quad (3.1)$$

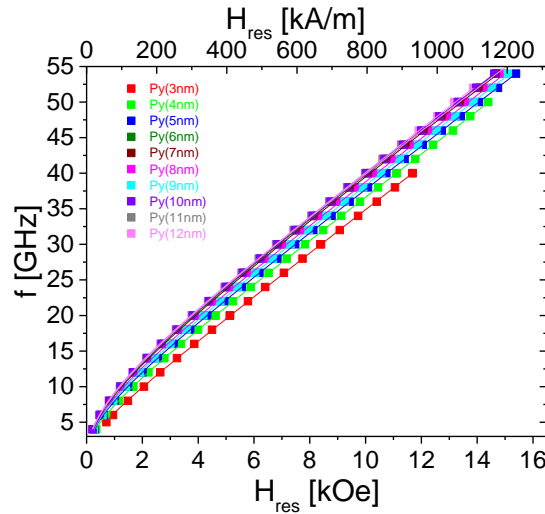


FIG. 3.1. Kittel plot for Si/SiO₂/Ni_{0.8}Fe_{0.2}/SiO₂ samples. Different colors represent different Ni_{0.8}Fe_{0.2} layer thicknesses.

For each sample, the effective magnetization (M_{eff}) and the gyromagnetic ratio (γ') is determined from the fit.

The effective magnetization $4\pi M_{eff} = 4\pi M_s - \frac{2K_u}{M_s}$ includes both shape anisotropy and the perpendicular anisotropy. $K_u > 0$ indicates that axis of this anisotropy contribution is normal to the film plane. In the general case that the perpendicular anisotropy K_u has both a volume contribution K_v and an interfacial contribution $K_{i,total}$ it can be written as [17]:

$$K_{eff} = (K_v - 2\pi M_s^2) + \frac{K_{i,total}}{t_{NiFe}}. \quad (3.2)$$

If both of the interfaces contribute to the interfacial anisotropy $K_{i,total}$ would be sum of the bottom interface contribution, $K_{i,bottom/NiFe}$, and top interface contribution, $K_{i,NiFe/top}$, contribution.

One can re-write Eq. (3.2) as:

$$4\pi M_{eff} = \left(4\pi M_s - \frac{2K_v}{M_s}\right) - \frac{2 K_{i,total}}{M_s t_{NiFe}} \quad (3.3)$$

Therefore, by fitting a straight line to $4\pi M_{eff}$ vs. $1/t_{NiFe}$ the value $4\pi M_s - \frac{2K_v}{M_s}$ can be extracted from the intercept and the effective interfacial anisotropy constant $K_{i,total}$ can be extracted from the slope. $4\pi M_{eff}$ vs. $1/t_{NiFe}$ data is shown in Fig. 3.2. The linearity of the data indicate that an interfacial perpendicular anisotropy is present in all of the samples. Assuming no bulk contribution to the perpendicular anisotropy ($K_v = 0$) for $Ni_{0.8}Fe_{0.2}$ [18], one can determine the saturation magnetization for $Ni_{0.8}Fe_{0.2}$ to be $M_s = 786 \pm 2 \text{ emu/cm}^3$. This value is consistent with the previously reported values that are within the range of $740 - 780 \text{ emu/cm}^3$ [16] for films with the same nominal stoichiometry.

However, more importantly, the data in Fig. 3.2 indicates that there is a strong interfacial perpendicular anisotropy in all samples. $K_{i,total}$ value is then $0.25 \pm 0.01 \text{ erg/cm}^2$, $0.54 \pm 0.01 \text{ erg/cm}^2$, and $0.75 \pm 0.01 \text{ erg/cm}^2$ for Si/SiO₂/Ru/Ni_{0.8}Fe_{0.2}/Ru, Si/SiO₂/Ni_{0.8}Fe_{0.2}/Ru, and Si/SiO₂/Ni_{0.8}Fe_{0.2}/SiO₂, respectively.

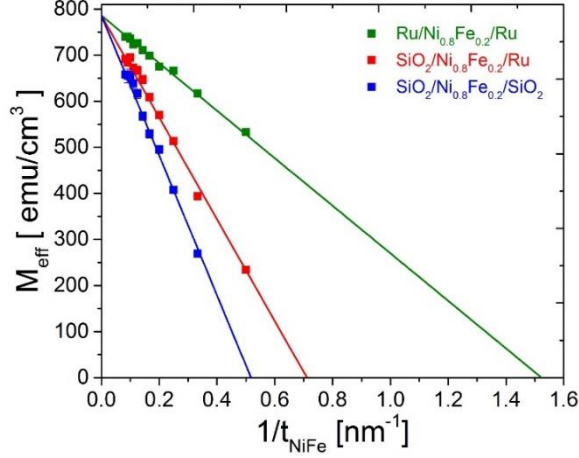


FIG. 3.2: M_{eff} vs. $1/t_{NiFe}$ for Si/SiO₂/Ni_{0.8}Fe_{0.2}/SiO₂ (blue symbols), Si/SiO₂/Ni_{0.8}Fe_{0.2}/Ru (red symbols), and Si/SiO₂/Ru/Ni_{0.8}Fe_{0.2}/Ru (green symbols). The lines are the fit to each data set.

and Si/SiO₂/Ni_{0.8}Fe_{0.2}/SiO₂, respectively. Since $K_{i,total} = K_{i,bottom/NiFe} + K_{i,NiFe/top}$ and

assuming that $K_{i,Ru/NiFe} = K_{i,NiFe/Ru} = K_{i,NiFe-Ru}$, and $K_{i,SiO_2/NiFe} = K_{i,NiFe/SiO_2} =$

$K_{i,NiFe-SiO_2}$, one obtains for the samples with the same top and bottom layers $K_{i,NiFe-Ru} =$

$0.13 \pm 0.01 \text{ erg/cm}^2$ and $K_{i,NiFe-SiO_2} = 0.37 \pm 0.01 \text{ erg/cm}^2$. This results suggest a strong

perpendicular interfacial anisotropy of the SiO₂-Ni_{0.8}Fe_{0.2} interface. The results of the

SiO₂/Ni_{0.8}Fe_{0.2}/Ru samples are consistent with these interfacial anisotropy contributions, the

experimental value of $K_{i,total}=0.54 \pm 0.01 \text{ erg/cm}^2$ with what one expects based on the results

of the samples with the same top and bottom layers agree within the error margins.

In addition to the high interfacial anisotropy that originates from the SiO₂/Ni_{0.8}Fe_{0.2} interface, using SiO₂ has an advantage over normal metals. Because of the short spin diffusion length in normal metals such as Ru the intrinsic damping parameter (effective Gilbert damping)

is enhanced as a result of angular momentum loss through spin pumping phenomena to the normal metal layer [19]. This is extremely important since fast dynamic response is essential in perpendicular media where lower damping material is advantageous [20]. Our results confirm that the effective Gilbert damping, α_{eff} , is enhanced for samples in which $\text{Ni}_{0.8}\text{Fe}_{0.2}$ has Ru buffer layers or Ru capping layers. α_{eff} vs. $1/t_{\text{NiFe}}$ data is presented in Fig. 3.3.

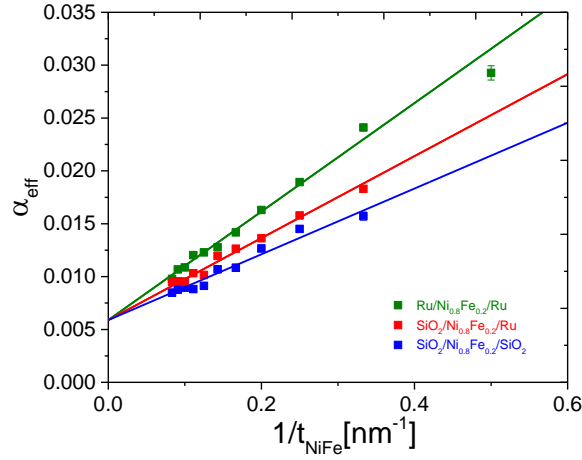


FIG. 3.3. Effective Gilbert damping vs. $1/t_{\text{NiFe}}$ for Si/SiO₂/ Ni_{0.8}Fe_{0.2} /SiO₂(blue symbols), Si/SiO₂/ Ni_{0.8}Fe_{0.2} /Ru (red symbols), and Si/SiO₂/Ru/ Ni_{0.8}Fe_{0.2} /Ru (green symbols).

From Fig. 3.3 one can extract the damping parameter for bulk $\text{Ni}_{0.8}\text{Fe}_{0.2}$ from the intercept of effective Gilbert damping parameter vs. $1/t_{\text{NiFe}}$ [19]. This value is calculated as 0.006 which is very close to the previously reported values for single crystal $\text{Ni}_{0.8}\text{Fe}_{0.2}$ [21]. To compare the spin-dependent transmission probabilities at interface, one can calculate the spin-mixing conductance using Eq. (3.4) [19]:

$$g_{\uparrow\downarrow,eff} = (\alpha - \alpha_0) \frac{2M_s t_{\text{NiFe}}}{\hbar\gamma'}. \quad (3.4)$$

In which α_0 is the intrinsic damping of the ferromagnet, \hbar is Planck's reduced constant and γ' is the effective gyromagnetic ratio. $g_{\uparrow\downarrow,eff}$ is $2.57 \times 10^{13} \text{ cm}^{-2}$, $1.97 \times 10^{13} \text{ cm}^{-2}$ for Si/SiO₂/Ru/ Ni_{0.8}Fe_{0.2} /Ru and Si/SiO₂/ Ni_{0.8}Fe_{0.2} /Ru respectively. Assuming the same

mechanism in Si/SiO₂/ Ni_{0.8}Fe_{0.2} /SiO₂ samples one would get $1.56 \times 10^{13} \text{ cm}^{-2}$. However, Eq. (3.4) is based on spin-injection into the adjacent layer and thus should not take place in the case where the adjacent layer is insulating. However, the $1/t_{NiFe}$ dependence of the effective Gilbert damping parameter clearly indicates an interfacial nature of the physical origin of the enhancement of the Gilbert damping parameter at the SiO₂/ Ni_{0.8}Fe_{0.2} interface.

Elevation angle dependent FMR measurements performed at a microwave frequency of 20GHz also reveal that the linewidth value is slightly higher when the applied magnetic field is perpendicular to the plane of the sample. Looking at the data presented in Fig. 3.4, one can see that the difference in the FMR linewidth for the in-plane and out-of-plane configurations is minimal when Ru is used as both underlayer and overlayer. Our data also suggests that the maximum difference for in-plane and out-of-plane configuration is when SiO₂ is used as both underlayer and overlayer.

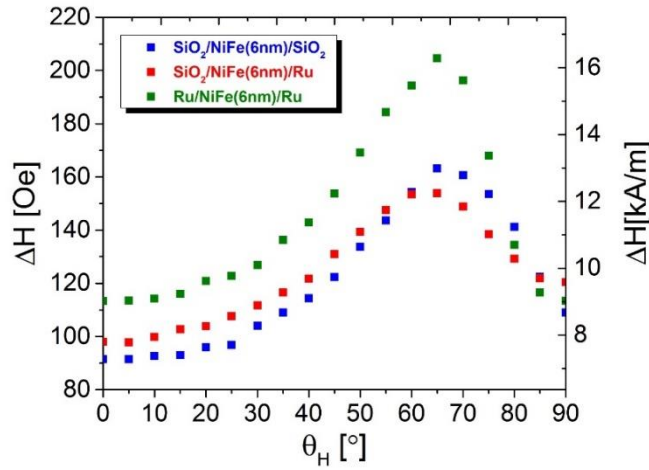


FIG. 3.4. Linewidth vs. elevation angle for Si/SiO₂/ Ni_{0.8}Fe_{0.2} (6nm)/SiO₂(blue symbols), Si/SiO₂/ Ni_{0.8}Fe_{0.2}(6nm) /Ru (red symbols), and Si/SiO₂/Ru/ Ni_{0.8}Fe_{0.2}(6nm) /Ru (green symbols). The microwave frequency was 20 GHz.

The increase of the linewidth in the out-of-plane configuration can be explained by inhomogeneous linewidth broadening that can be caused by variations of the perpendicular

interfacial anisotropy [23]. Variation of perpendicular anisotropy due to interface morphology leads to higher FMR linewidth for the out-of-plane configuration.

IV. Conclusion

We have investigated interfacial perpendicular anisotropy in sputter deposited $\text{Ni}_{0.8}\text{Fe}_{0.2}$ films in three configurations that are $\text{Si}/\text{SiO}_2/\text{Ni}_{0.8}\text{Fe}_{0.2}/\text{SiO}_2$, $\text{Si}/\text{SiO}_2/\text{Ni}_{0.8}\text{Fe}_{0.2}/\text{Ru}$, and $\text{Si}/\text{SiO}_2/\text{Ru}/\text{Ni}_{0.8}\text{Fe}_{0.2}/\text{Ru}$. Our results reveal a strong perpendicular interfacial anisotropy at the $\text{Ni}_{0.8}\text{Fe}_{0.2}/\text{SiO}_2$ interface. In addition, the FMR linewidth analysis confirms higher FMR linewidth for out-of-plane configuration when $\text{Ni}_{0.8}\text{Fe}_{0.2}/\text{SiO}_2$ interface contributes to the interfacial anisotropy. This is explained by inhomogeneous linewidth broadening which can be a result of variations in the interfacial perpendicular anisotropy. Our FMR results also confirm that the Gilbert damping parameter is smaller when $\text{Ni}_{0.8}\text{Fe}_{0.2}$ is in proximity of SiO_2 other than the Ru layer. Achieving a smaller Gilbert damping parameter is of particular importance in device applications such as STT-MRAM.

V. Acknowledgements

This work was supported by NSF-CAREER Award No. 0952929 and by NSF-CAREER Award No. 1452670.

VI. References

- [1] K. Lee, J.J. Sapan, S.H. Kang, and E.E. Fullerton, Perpendicular magnetization of CoFeB on single-crystal MgO, *Journal of Applied Physics* 109, 123910 (2011), doi:<http://dx.doi.org/10.1063/1.3592986>.
- [2] F. Huang, G.J. Mankey, and R.F. Willis, Interfacial anisotropy and magnetic transition of cobalt films on Cu(111), *Journal of Applied Physics* 75, 6406 (1994), 10.1063/1.355366.
- [3] Z. Wen, H. Sukegawa, T. Furubayashi, J. Koo, K. Inomata, S. Mitani, J.P. Hadorn, T. Ohkubo, and K. Hono, A 4-Fold-Symmetry Hexagonal Ruthenium for Magnetic Heterostructures Exhibiting Enhanced Perpendicular Magnetic Anisotropy and Tunnel Magnetoresistance, *Advanced Materials* 26, 6483 (2014), 10.1002/adma.201401959.
- [4] S. Bandiera, R.C. Sousa, B. Rodmacq, and B. Dieny, Asymmetric Interfacial Perpendicular Magnetic Anisotropy in Pt/Co/Pt Trilayers, *IEEE Magnetics Letters* 2, 3000504 (2011), 10.1109/LMAG.2011.2174032.
- [5] M. Kim, S. Kim, J. Ko, and J. Hong, Contribution of individual interfaces in the MgO/Co/Pd trilayer to perpendicular magnetic anisotropy upon annealing, *Applied Physics Letters* 106, 102404 (2015), doi:<http://dx.doi.org/10.1063/1.4914497>.
- [6] S. Peng, M. Wang, H. Yang, L. Zeng, J. Nan, J. Zhou, Y. Zhang, A. Hallal, M. Chshiev, K.L. Wang, Q. Zhang, and W. Zhao, Origin of interfacial perpendicular magnetic anisotropy in MgO/CoFe/metallic capping layer structures, 5, 18173 (2015), 10.1038/srep18173 <http://www.nature.com/articles/srep18173#supplementary-information>.
- [7] S. Mizukami, Y. Ando, and T. Miyazaki, Effect of spin diffusion on Gilbert damping for a very thin permalloy layer in Cu/permalloy/Cu/Pt films, *Physical Review B* 66, 104413 (2002), <http://link.aps.org/doi/10.1103/PhysRevB.66.104413>.
- [8] P. Djemia, F. Ganot, and P. Moch, Symposium E: Magnetic Ultrathin Films, Multilayers and Surfaces Brillouin scattering in ultrathin permalloy films: monolayers and multilayers with alumina interfaces, *Journal of Magnetism and Magnetic Materials* 165, 428 (1997), [http://dx.doi.org/10.1016/S0304-8853\(96\)00577-X](http://dx.doi.org/10.1016/S0304-8853(96)00577-X).
- [9] Y.-W. Oh, K.-D. Lee, J.-R. Jeong, and B.-G. Park, Interfacial perpendicular magnetic anisotropy in CoFeB/MgO structure with various underlayers, *Journal of Applied Physics* 115, 17C724 (2014), doi:<http://dx.doi.org/10.1063/1.4864047>.
- [10] H. Lee, L. Wen, M. Pathak, P. Janssen, P. LeClair, C. Alexander, C.K.A. Mewes, and T. Mewes, Spin pumping in Co 56 Fe 24 B 20 multilayer systems, *Journal of Physics D: Applied Physics* 41, 215001 (2008), <http://stacks.iop.org/0022-3727/41/i=21/a=215001>.

- [11] S. Ikeda, K. Miura, H. Yamamoto, K. Mizunuma, H.D. Gan, M. Endo, S. Kanai, J. Hayakawa, F. Matsukura, and H. Ohno, A perpendicular-anisotropy CoFeB–MgO magnetic tunnel junction, *Nat Mater* 9, 721 (2010), <http://dx.doi.org/10.1038/nmat2804>.
- [12] Y. Cui, B. Khodadadi, S. Schäfer, T. Mewes, J. Lu, and S.A. Wolf, Interfacial perpendicular magnetic anisotropy and damping parameter in ultra thin Co₂FeAl films, *Applied Physics Letters* 102, 162403 (2013), doi:<http://dx.doi.org/10.1063/1.4802952>.
- [13] A. Manchon, S. Pizzini, J. Vogel, V. Uhlîr, L. Lombard, C. Ducruet, S. Auffret, B. Rodmacq, B. Dieny, M. Hochstrasser, and G. Panaccione, X-Ray analysis of the magnetic influence of oxygen in PtCo/AlO_x trilayers, *Journal of Applied Physics* 103, 07A912 (2008), doi:<http://dx.doi.org/10.1063/1.2829896>.
- [14] J. Okabayashi, J.W. Koo, H. Sukegawa, S. Mitani, Y. Takagi, and T. Yokoyama, Perpendicular magnetic anisotropy at the interface between ultrathin Fe film and MgO studied by angular-dependent x-Ray magnetic circular dichroism, *Applied Physics Letters* 105, 122408 (2014), doi:<http://dx.doi.org/10.1063/1.4896290>.
- [15] J.O. Rantschler, P.J. Chen, A.S. Arrott, R.D. McMichael, W.F. Egelhoff, and B.B. Maranville, Surface anisotropy of permalloy in NMNiFeNM multilayers, *Journal of Applied Physics* 97, 10J113 (2005), doi:<http://dx.doi.org/10.1063/1.1853711>.
- [16] T. Kamada, T. Kubota, S. Takahashi, Y. Sonobe, and K. Takanashi, Perpendicular Magnetic Anisotropy of Co₂Fe_xMn_{1-x}Si Heusler Alloy Ultra-Thin Films, *IEEE Transactions on Magnetics* 50, 1 (2014), 10.1109/TMAG.2014.2322857.
- [17] C.-H. Lambert, A. Rajanikanth, T. Hauet, S. Mangin, E.E. Fullerton, and S. Andrieu, Quantifying perpendicular magnetic anisotropy at the Fe-MgO(001) interface, *Applied Physics Letters* 102, 122410 (2013), doi:<http://dx.doi.org/10.1063/1.4798291>.
- [18] L.F. Yin, D.H. Wei, N. Lei, L.H. Zhou, C.S. Tian, G.S. Dong, X.F. Jin, L.P. Guo, Q.J. Jia, and R.Q. Wu, Magnetocrystalline Anisotropy in Permalloy Revisited, *Physical Review Letters* 97, 067203 (2006), <https://link.aps.org/doi/10.1103/PhysRevLett.97.067203>.
- [19] Y. Tserkovnyak, A. Brataas, G.E.W. Bauer, and B.I. Halperin, Nonlocal magnetization dynamics in ferromagnetic heterostructures, *Reviews of Modern Physics* 77, 1375 (2005), <http://link.aps.org/doi/10.1103/RevModPhys.77.1375>.
- [20] C.S. Rizal and Y. Ueda, Magnetoresistance and Magnetic Anisotropy Properties of Strain-Induced Co/Ag Multilayer Films, *IEEE Transactions on Magnetics* 45, 2399 (2009), 10.1109/TMAG.2009.2018588.
- [21] K. Kobayashi, N. Inaba, N. Fujita, Y. Sudo, T. Tanaka, M. Ohtake, M. Futamoto, and F. Kirino, Damping Constants for Permalloy Single-Crystal Thin Films, *IEEE Transactions on Magnetics* 45, 2541 (2009), 10.1109/TMAG.2009.2018862.

[22] T. Qu, S.C. Pandey, G.S. Sandhu, and R.H. Victora, Theoretical Study of Magnetic Damping and Anisotropy of Fe/Pd (001) Superlattice, IEEE Transactions on Magnetics 52, 1 (2016), 10.1109/TMAG.2015.2514260.

[23] R.D. McMichael, D.J. Twisselmann, and A. Kunz, Localized Ferromagnetic Resonance in Inhomogeneous Thin Films, Physical Review Letters 90, 227601 (2003), <http://link.aps.org/doi/10.1103/PhysRevLett.90.227601>.

4. INHOMOGENEOUS PERPENDICULAR MAGNETIC ANISOTROPY AS A SOURCE OF HIGHER-ORDER QUASI-STATIC AND DYNAMIC ANISOTROPIES

J. B. Mohammadi¹, K. Cole¹, T. Mewes¹, C. K. A. Mewes¹

¹*Department of Physics and Astronomy, MINT Center,*

The University of Alabama, Tuscaloosa, Alabama 35487, USA

We investigate the influence of lateral variations of the second-order perpendicular anisotropy in thin films on the effective anisotropies required to represent this structure using a macrospin approximation. Second-order and fourth-order effective anisotropies are required for the macrospin approximation. In the case of quasi-static calculations, the fourth-order effective anisotropy is closely linked to deviations of the average magnetization angle from the field direction and lateral variations of the magnetization direction in the structure leading to dependence on the field strength and the lateral length scale of anisotropy variations of the effective anisotropies. We find that the field and lateral length scale dependence of the effective anisotropies extracted from simulations of the magnetization dynamics are profoundly different from those of the quasi-static simulations. This is caused by resonance localization that depends on the orientation of the external magnetic field.

I. Introduction

The presence of a strong perpendicular anisotropy is of significant importance for materials intended for use in spintronic devices. For example, a significant reduction of the switching current density while maintaining the thermal stability for spin transfer torque magnetic random-access memories (STT-MRAM) can be achieved by utilizing a perpendicular anisotropy [1,2]. One common observation in these materials is that in order to accurately describe their quasi-static or dynamic properties one has to include both second-order (K_2) and fourth-order uniaxial anisotropy (K_4) contributions to the anisotropy energy density E_{aniso} [3-7]:

$$E_{aniso} = K_2 \cdot \cos^2 \theta_M + \frac{K_4}{2} \cdot \cos^4 \theta_M \quad (4.1)$$

where θ_M is the angle of the magnetization with respect to the film normal. We note that the nomenclature for the anisotropy constants is inconsistent in the literature, as they are also referred to as first-order and second-order anisotropy constants. With the above definition, the film normal is an easy axis of the corresponding anisotropy contribution for $K_i < 0$, but the opposite sign convention is also commonly used in the literature.

By using a second order perturbation of the tight binding model, Bruno was able to show the connection of the asymmetry in the orbital moment and the second-order anisotropy K_2 [8]. However, currently a clear theoretical picture for the origin of the fourth-order anisotropy K_4 is lacking. While recent fully-relativistic ab initio calculations have shown the presence of such a term, its magnitude was only 3% of the second-order anisotropy [9]. However, using analytical models it has been shown that lateral fluctuations of the second-order perpendicular anisotropy can lead to the emergence of higher order anisotropy terms [10,11]. Here we report on detailed micromagnetic investigations of lateral variations of the second-order

perpendicular anisotropy and its influence on the effective anisotropies and the magnetization dynamics of thin films.

The manuscript is structured as follows. First we start with a description of the theoretical background and explanation of the methodology relevant for the micromagnetic calculations and their analysis in the framework of a macrospin model. In the next section, we discuss the quasi-static properties of the system, starting with a detailed discussion of the angular dependence of the different contributions to the energy of the system and how they contribute to the effective anisotropies that are required when representing the system with a macrospin model. We also investigate the field dependence of the effective anisotropies [12]. In the subsequent section, we discuss the influence of the length scale of the lateral variations of the second-order anisotropy on the effective anisotropies. After this we analyze the dynamic properties of the system and compare their dependence on the length scale of the lateral variations of the second-order uniaxial anisotropy with those of the quasi-static properties. We conclude with a summary and discussion of our results.

II. Results and discussion

A. Theoretical background (Methodology)

For the micromagnetic modeling we use our finite differences code M^3 [13] written in the MATLAB scripting language. M^3 uses a fast Fourier transform (FFT) method to calculate the magnetostatic interactions. M^3 utilizes Newell's formulation to calculate the demagnetizing tensor at short distances [14] and a dipole approximation for the far field. For the current work, we used the 6-neighbor method for the exchange interaction and Neuman boundary conditions [15].

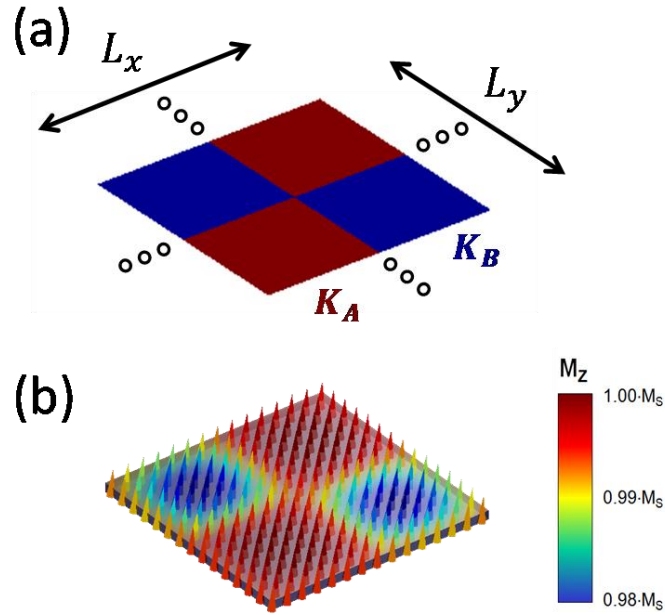


FIG. 4.1. (a) Periodic checkerboard pattern used for the simulations, regions A have a second-order perpendicular anisotropy $K_{2,A} = -1.5 \times 10^6 \text{ J/m}^3$ whereas for regions B $K_{2,B} \geq 0$. (b) Relaxed magnetization with an external magnetic field of $\mu_0 H = 1 \text{ T}$ applied at an angle of $\theta_H = 5^\circ$ with respect to the film normal.

For the simulations, the perpendicular magnetic anisotropy is assumed to be constant across the film thickness, i.e. in our model we use the thickness-averaged perpendicular anisotropy. However, the model takes into account lateral variations of this thickness-averaged perpendicular anisotropy, which could for example be caused by lateral variations of the strength of the interfacial perpendicular anisotropy or by lateral variations of the film thickness. Instead of attempting to model a specific system, for which one would have to make assumptions about the details of the interfacial roughness and its influence on the length scale and amplitude of the lateral variations of the perpendicular anisotropy, our aim is to capture the basic physics by using a simplified model.

Our model incorporates lateral variations of the second-order uniaxial anisotropy in the form of a periodic checkerboard structure, as pictured in Fig. 4.1. For all simulations regions A

have a second-order perpendicular anisotropy, $K_{2,A} = -1.5 \times 10^6 \text{ J/m}^3$, which is sufficient to overcome the demagnetizing field and thus results in an easy axis of these regions along the film normal. While the strength of the second-order perpendicular anisotropy $K_{2,B} \geq 0$ of regions B was varied for different simulations, the film normal for these regions is always a hard axis. In the micromagnetic simulations both regions have no intrinsic fourth-order uniaxial anisotropy, i.e. $K_{4,A} = K_{4,B} = 0$. However, as will be shown below, the frustration between these two regions caused by their different second-order uniaxial anisotropies leads to the emergence of a fourth-order anisotropy contribution of the system when analyzed in the macrospin approximation. For the saturation magnetization of the system we chose $M_S = 1000 \text{ kA/m}$, while the exchange constant was set to $A = 1 \times 10^{-11} \text{ J/m}$. The wavelength $L_{x,y}$ of the pattern was chosen to be the same along both in-plane directions and for the following discussion was set to $L_x = L_y = 30 \text{ nm}$. The influence of the length scale of the lateral anisotropy variations is investigated in detail in section C.

B. Quasi-static properties

To determine the quasi-static properties of the system, an external magnetic field \vec{H} is applied at different angles θ_H with respect to the film normal. After relaxing the system, the magnetization is generally aligned along the applied field direction. However, a close inspection shows that the degree of alignment differs in the two regions, as shown in Fig. 4.1 (b). To quantitatively analyze these simulations, we calculate the average angle of the magnetization $\theta_M = \frac{1}{N} \sum_i \theta_{M,i}$ with respect to the film normal and the different contributions to the total energy density of the relaxed structure averaged over all N cells in the simulation volume. The total energy density of the system is the sum of the demagnetizing energy (dipole-dipole interaction), the anisotropy, the Zeeman energy, and the exchange energy:

$$E_{total} = E_{demag} + E_{anisotropy} + E_{Zeeman} + E_{exchange} \quad (4.2)$$

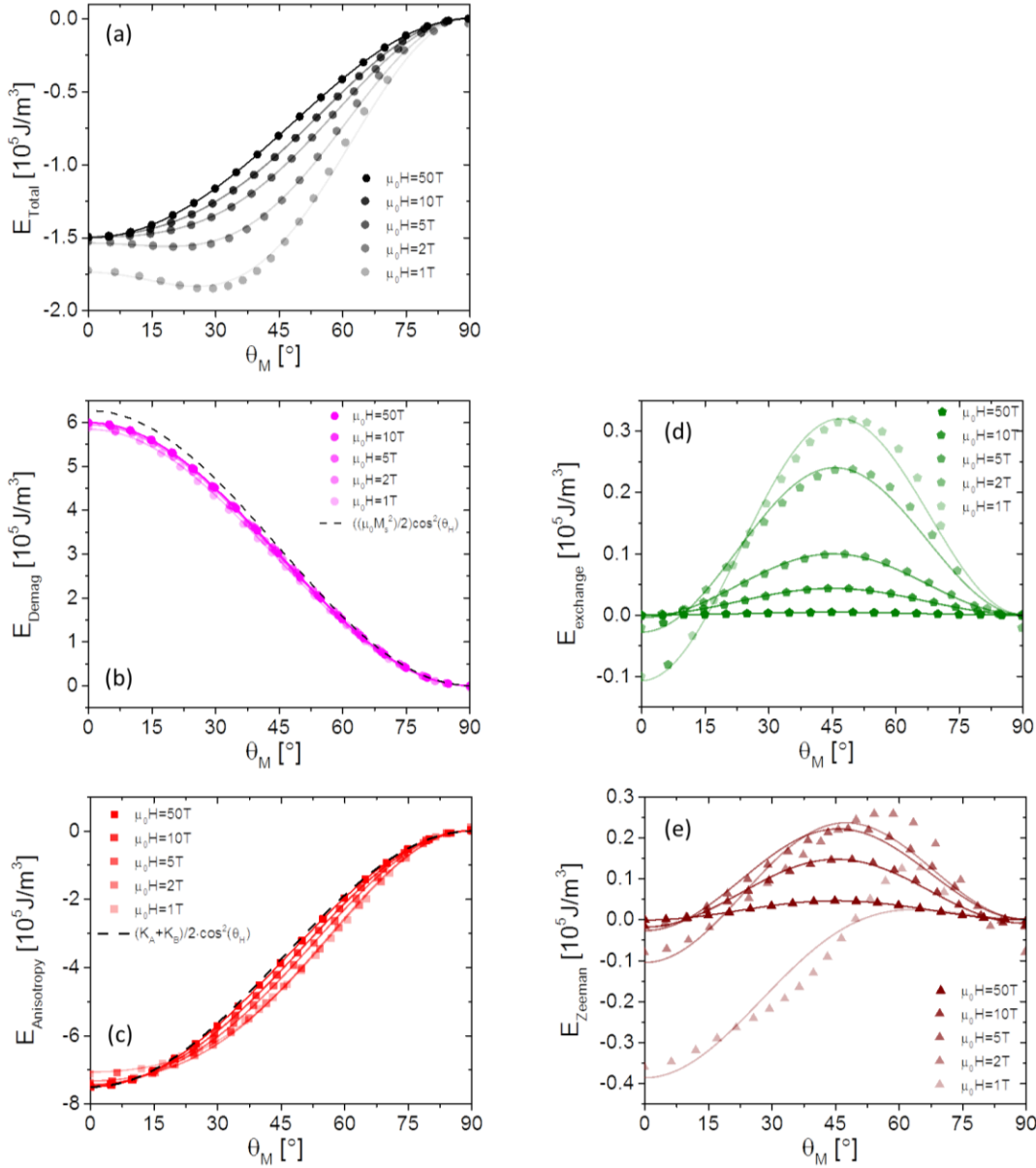


FIG. 4.2. Dependence of (a) the total energy density, (b) the demagnetizing energy density, (c) the anisotropy energy, (d) the exchange energy density and (e) the Zeeman energy density on the average magnetization angle θ_M obtained after relaxing the magnetization with the indicated external magnetic field applied at different angles. The solid lines are a fit using the macrospin model, see Eq. (4.3). The dashed lines in (b) and (c) represent the expected angular dependence for the demagnetizing energy density of an infinite thin film and the volume averaged anisotropy energy density respectively.

In Fig. 4.2, the total energy density and the individual contributions are shown as a function of the average angle of the magnetization for a perpendicular second-order anisotropy in

regions A of $K_{2,A} = -1.5 \times 10^6 \text{ J/m}^3$ and a second-order anisotropy in regions B of $K_{2,B} = 0 \text{ J/m}^3$. For these simulations, the applied magnetic field was varied from $\mu_0 H = 1 \text{ T}$ to 50 T . As can be seen in Fig. 4.2 (a) for applied fields less than 2 T the total energy density of the system has maxima along the out-of-plane ($\theta_M = 0^\circ$) and the in-plane ($\theta_M = 90^\circ$) orientations of the magnetization and a minimum at an intermediate angle. This is a clear indication that a higher-order anisotropy term will be required to describe this system using a macrospin approximation, although the microscopic model did not include such a term. The solid lines in Fig. 4.2 (a) show a fit to the simulation results using both a second-order and fourth-order anisotropy contribution:

$$E = E_0 + \tilde{K}_{2,eff} \cdot \cos^2 \theta_M + \frac{K_{4,eff}}{2} \cdot \cos^4 \theta_M \quad (4.3)$$

where we use effective quantities to indicate a macrospin representation of the system. The effective anisotropy $\tilde{K}_{2,eff}$ in Eq. (4.3) contains both shape anisotropy and the uniaxial anisotropy contributions. In particular, for an infinite, homogeneously magnetized thin film one could separate these two contributions as follows: $\tilde{K}_{2,eff} = \frac{\mu_0 M_s^2}{2} + K_{2,eff}$. However, in the case of lateral variations of the microscopic second-order perpendicular anisotropy K_2 the film is not homogeneously magnetized (see Fig. 4.3 (b)) and thus the shape anisotropy contribution to $\tilde{K}_{2,eff}$ is expected to be reduced from the value for an infinite film. This can be seen in Fig. 4.2 (b) where E_{demag} , the energy contribution due to dipole-dipole interaction in the structure is shown separately as a function of the average magnetization angle. For comparison, we also show the expectation for the angular dependence of this contribution for a homogeneously magnetized thin film ($\frac{\mu_0 M_s^2}{2} \cdot \cos^2 \theta_M$, dashed line). The main difference between the micromagnetic and the analytical result for a homogeneously magnetized thin film is indeed a

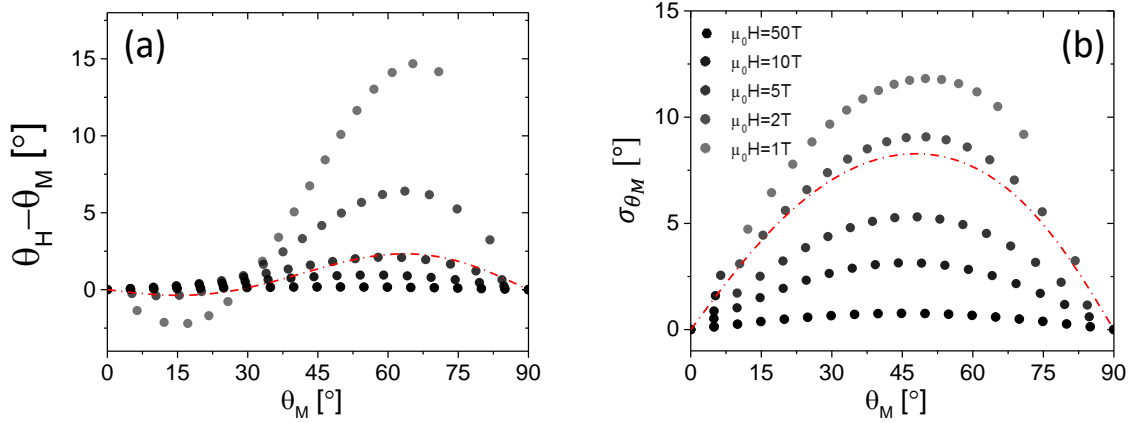


FIG. 4.3. (a) Deviation of the average angle of the magnetization θ_M from the angle of the applied field θ_H shown as a function of the average angle of the magnetization θ_M . The symbols represent the results from micromagnetic simulations with different strengths of the applied field. The red dash dotted line is the result obtained by ignoring exchange interaction and treating each region as a separate macrospin for an applied field $\mu_0 H = 5T$. (b) Standard deviation σ_{θ_M} of the magnetization angle from its average orientation θ_M as a function of the same. The symbols represent the results from micromagnetic simulations with different strengths of the applied field. The red dash dotted line is the result obtained by ignoring exchange interaction and treating each region as a separate macrospin for an applied field $\mu_0 H = 5T$, here the difference between the angle of the magnetization in region A and B is shown.

small reduction of the amplitude of the second-order uniaxial anisotropy. However, we also observe that a fourth-order contribution is required to fit the angular dependence of the energy contribution of the dipole-dipole interaction using Eq. (4.3). With increasing external magnetic field, the magnetization in the structures becomes more homogenous (Fig. 4.3 (b)) and thus the effective second-order uniaxial anisotropy approaches the thin film limit (see Fig. 4.4(a)) and the fourth-order anisotropy contribution diminishes (see Fig. 4.4 (b)).

In Fig. 4.2 (c), we show the anisotropy contribution to the total energy density of the system as a function of the magnetization angle. For comparison, the angular dependence of the anisotropy contribution of a homogeneously magnetized thin film with a second-order uniaxial anisotropy

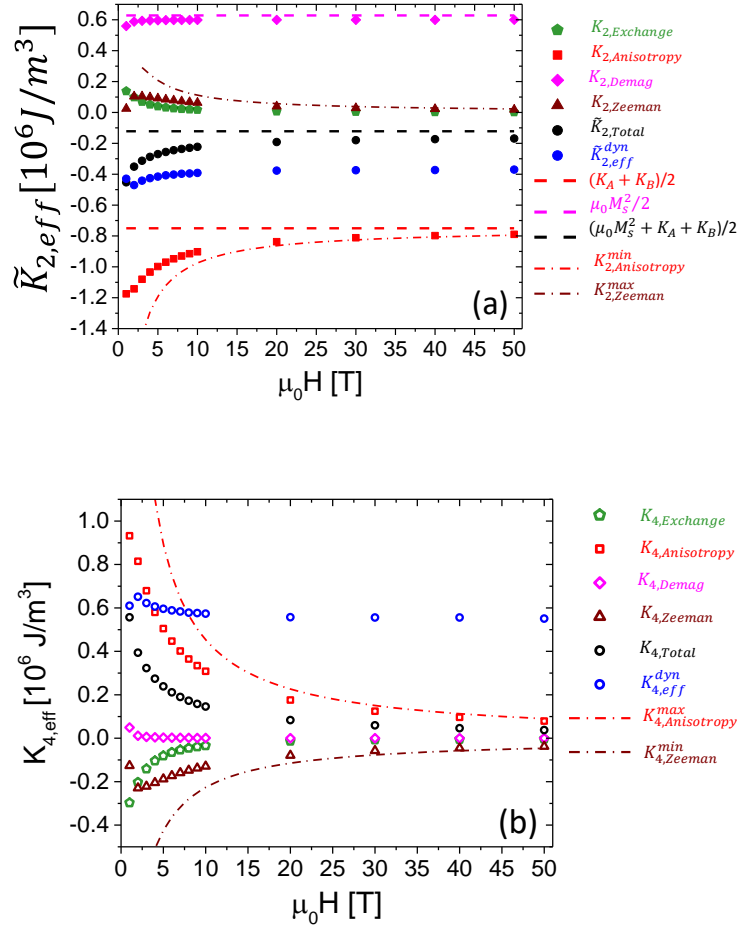


FIG. 4.4. (a) Field dependence of the effective second-order uniaxial anisotropy determined by fitting Eq. (4.3) to the angular dependence of the different contributions to the total energy, cp. Fig. 4.2. The dashed red line is the volume averaged second-order uniaxial anisotropy. The pink dashed line represents the demagnetization energy density for a homogenously magnetized infinite film. The dash dotted red line is the anisotropy contribution to the effective second-order uniaxial anisotropy obtained by ignoring exchange interactions between the regions and treating them each as a macrospin. The dark red dash dotted line is the Zeeman contribution to the effective second-order anisotropy using the same simplified model. (b) Field dependence of the effective fourth-order uniaxial anisotropy. The dash dotted red lines represent contribution obtained by ignoring exchange interactions between the regions and treating them each as a macrospin, the anisotropy and Zeeman contribution are shown in red and dark red respectively. The blue symbols in both graphs are the effective anisotropies determined from dynamical calculations, see section D.

equal to the volume averaged anisotropy of the two regions $\bar{K}_{2,eff} = \frac{K_{2,A} + K_{2,B}}{2} = -0.75 \times 10^6 \text{ J/m}^3$ is also shown (dashed line). One notes that the energy difference between the out-of-plane easy axis and the in-plane hard axis is well approximated by the volume average $\bar{K}_{2,eff}$.

However, a significant fourth-order anisotropy $K_{4,eff}$ is required to fit this energy contribution using Eq. (4.3). Because the fourth-order contribution has the opposite sign compared to the second-order contribution, this causes the second-order anisotropy $\tilde{K}_{2,eff}$ extracted from the fit to be smaller than the volume averaged anisotropy, i.e. $\tilde{K}_{2,eff} < \bar{K}_{2,eff}$. With increasing external applied field, the effective second-order anisotropy of this contribution approaches the volume average $\bar{K}_{2,eff}$ (see Fig. 4.4 (a)), whereas the fourth-order contribution $K_{4,eff}$ approaches zero (see Fig. 4.4 (b)). Again, this is caused by the reduction of the inhomogeneity of the magnetization with increasing magnetic field (see Fig. 4.3 (b)).

In Fig. 4.2 (d) we show the exchange contribution to the total energy density of the system as a function of the magnetization angle. At high fields this contribution closely follows the angular dependence of the inhomogeneity of the magnetization as shown in Fig. 4.3 (b). However, at low fields the average magnetization of the structure is not well aligned with the direction of the external magnetic field (see Fig. 4.3 (a)) leading to a more complicated magnetization distribution and thus a more complex angular dependence of the exchange contribution. As shown in Fig. 4.2 (d), this energy contribution can again be reasonably fitted using Eq. (4.3). The second-order uniaxial anisotropy contribution due to exchange interaction is positive, while the fourth-order contribution is negative but comparable in magnitude. Both contributions diminish with increasing external magnetic field (see Fig. 4.4 (a) and (b)).

Finally, in Fig. 4.2 (e) the angular dependence of the Zeeman contribution to the total energy of the system is shown. The angular dependence of this energy contribution is mainly caused by the angular dependence of the deviation of the magnetization from the field direction (see Fig. 4.3 (a)) while the inhomogeneity of the magnetization only plays a minor role. We would like to point out that even for a system with no lateral variations of the second-order uniaxial anisotropy, i.e. $K_{2,A} = K_{2,B}$, the system will show a similar angular dependence as the one in Fig. 4.2 (e) for the Zeeman contribution to the total energy. This is because for finite external fields applied other than along the film normal ($\theta_H = 0^\circ$) or in the film plane ($\theta_H = 90^\circ$) the magnetization is never fully aligned with the field direction. The description of the angular dependence shown in Fig. 4.2 (e) using Eq. (4.3) does not capture some of the more complex behavior at low fields caused by large changes and variations of the magnetization direction. However, the agreement of the fit using Eq. (4.3) significantly improves with increasing field. Like the exchange contribution, the Zeeman contribution leads to a positive second-order and a negative fourth-order uniaxial anisotropy contribution (see Fig. 4.4 (a) and (b)). The magnitude of both contributions is comparable to the exchange contributions. However, the Zeeman contribution to the fourth-order uniaxial anisotropy drops off slower with the applied field than the exchange contribution, see Fig. 4.4 (b).

Fig. 4.4 (a) and (b) provide a visual summary of the results discussed in this section. Lateral variations of the second-order uniaxial anisotropy lead to the presence of a fourth-order uniaxial anisotropy, if one attempts to describe the system using a macrospin approximation. The main contributions to the total effective anisotropies are caused by the anisotropy contribution to the total energy. The total effective fourth-order anisotropy has the opposite sign as the total effective second-order anisotropy, which is a requirement for easy cone [16-18], that are often

observed experimentally. The effective anisotropies show a complex field dependence that can be understood by considering all contributions to the energy of the system, as discussed in detail in this section. Also shown in Fig. 4.4 (a) & 4.4 (b) as dash-dotted lines ($K_{2,Anisotropy}^{min}$ & $K_{2,Zeeman}^{max}$ in (a) and $K_{4,Anisotropy}^{max}$ & $K_{4,Zeeman}^{min}$ (b)) is the asymptotic behavior one expects by treating both regions separately as macrospins and ignoring exchange interaction. As can be seen in these figures, the micromagnetic results approach this asymptotic behavior for very large magnetic fields, well beyond what can typically be achieved experimentally.

C. Influence of length scale of lateral anisotropy variations

So far, we have discussed the case of variations of the second-order uniaxial anisotropy for a fixed wavelength $L_x = L_y$. However, in physical samples one expects, for example interfacial roughness to lead to variations of the second-order uniaxial anisotropy over a continuum of length scales. For the following discussion, we use the same simulation parameters as in the previous section, but now change the length scale of the lateral variations of the second-order uniaxial anisotropy.

In Fig. 4.5 (a) and 4.5 (b) we show the results of quasi-static simulations carried out in an external magnetic field $\mu_0 H = 5 T$. As discussed previously the angular dependence of the individual energy contributions was fitted using the macrospin model description of Eq. (4.3). As expected for anisotropy fluctuations on short length scales the energy contribution due to dipole-dipole interaction leads to a significantly lower effective second-order uniaxial anisotropy $\tilde{K}_{2,eff}$ contribution than one expects for a homogeneously magnetized film (dashed magenta line in Fig. 4.5 (a)). However, as the length scale of the anisotropy fluctuations increases the effective second-order uniaxial anisotropy contribution due to dipole-dipole interaction approaches this

value. As mentioned previously, the fourth-order uniaxial anisotropy contribution due to dipole-dipole interaction is small, given that the applied field is sufficiently large.

The anisotropy contribution to the effective second-order uniaxial anisotropy approaches the volume average $\bar{K}_{2,eff} = \frac{K_{2,A}+K_{2,B}}{2}$ (red dashed line in Fig. 4.5 (a)) for anisotropy fluctuations over very short length scales. This is expected, because in this case the exchange interaction dominates and forces the moments in neighboring regions to be parallel, thereby effectively averaging over them. The decrease of the effective second-order uniaxial anisotropy $\tilde{K}_{2,eff}$ with increasing length-scale of the anisotropy fluctuations is correlated with the increase of the fourth-order uniaxial anisotropy contribution. As discussed in the previous section this fourth-order contribution is driven by the inhomogeneity of the magnetization, which vanishes along the in-plane and out-of-plane orientation of the applied field. However, for any other angle of the applied field, the magnetization varies spatially. With increasing length scale of the lateral anisotropy fluctuations this inhomogeneity increases, as neighboring regions are less rigidly coupled, therefore leading to an increase of the effective fourth-order uniaxial anisotropy contribution. Furthermore, the energy difference between these in-plane and out-of-plane field orientations is always given by the volume average $\bar{K}_{2,eff}$, because in these two orientations the magnetization is homogenous and aligned along the magnetic field direction (see Fig. 4.3 (a) & 4.3 (b)). Therefore, with increasing length scale of the anisotropy fluctuations the effective second-order uniaxial anisotropy decreases as the fourth-order uniaxial anisotropy increases. Both effective anisotropies extracted from the full micromagnetic model approach the values expected based on treating the individual regions as macrospins and ignoring the exchange interaction. See the dash-dotted lines for $K_{2,Anisotropy}^{min}$ in Fig. 4.5 (a) and for $K_{4,Anisotropy}^{max}$ in Fig. 4.5 (b).

Due to the large applied magnetic field, the contribution of the exchange interaction to both the effective second-order and fourth-order uniaxial anisotropy remain relatively small over the entire range of the length scales investigated. For very short length scales of the lateral anisotropy fluctuations the contributions are small because neighboring regions are rigidly coupled to each other. For very large length scales on the other hand the contributions due to the exchange interaction diminish because the individual regions are homogeneously magnetized and only the boundaries between them lead to an angle dependent exchange interaction contribution to the total energy of the system. At intermediate length scales, this leads to a maximum for the effective second-order uniaxial anisotropy (Fig. 4.5 (a)) and to a minimum for the effective fourth-order uniaxial anisotropy (Fig. 4.5 (b)).

On the other hand, the large applied magnetic field combined with the deviation of the magnetization direction from the applied field direction, as discussed in the previous section, also leads to an angular dependence of the Zeeman contribution to the energy of the system. With increasing length scale of the lateral anisotropy variations, the effective second and fourth-order anisotropies of the full micromagnetic model approach the values expected based on treating the individual regions as macrospins and ignoring the exchange interaction, see the dash-dotted lines for $K_{2,Zeeman}^{max}$ in Fig. 4.5 (a) and for $K_{4,Zeeman}^{min}$ in Fig. 4.5 (b).

In summary, the total effective fourth-order anisotropy caused by large scale lateral variations of the second-order anisotropy has two main contributions: from the Zeeman and the anisotropy contribution to the total energy of the system. As can be seen in Fig. 4.5 (b) these two contributions have opposite signs. For lateral variations, over shorter length scales the exchange interaction also contributes significantly to the total effective fourth-order anisotropy of the

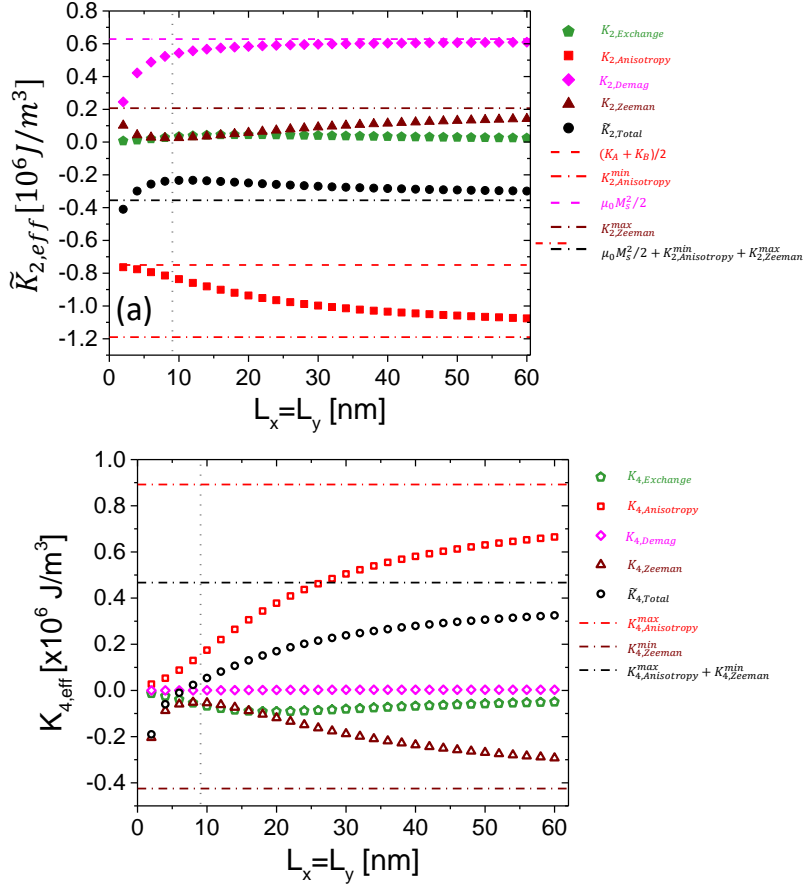


FIG. 4.5. (a) Dependence of the effective second-order uniaxial anisotropy on the lateral length scale of the second-order anisotropy variations. The dashed red line is the volume averaged second-order uniaxial anisotropy. The pink dashed line represents the demagnetization energy density for a homogenously magnetized infinite film. The dash dotted red line is the anisotropy contribution to the effective second-order uniaxial anisotropy obtained by ignoring exchange interactions between the regions and treating them each as a macrospin. The dark red dash dotted line is the Zeeman contribution to the effective second-order anisotropy using the same simplified model. The black dash dotted line is the sum of demagnetization energy, the anisotropy and Zeeman contribution in the macrospin approximation. (b) Dependence of the effective fourth-order uniaxial anisotropy on the lateral length scale of the second-order anisotropy variations. The dash dotted red lines represent contribution obtained by ignoring exchange interactions between the regions and treating them each as a macrospin, the anisotropy and Zeeman contribution are shown in red and dark red respectively. The black dash dotted line is the sum of these contributions. The gray vertical dashed lined is the length scale λ_{eff} , see text for details.

system. Furthermore, in this case the contribution of the dipole-dipole interaction to the effective second-order anisotropy deviates significantly from the thin film limit and thus needs to

be taken into account. Finally, we can compare the variations seen in Fig. 4.5 with characteristic length scales of the system. For the system discussed here, the demagnetizing energy results in a characteristic length of $\lambda_d = \sqrt{2A/(\mu_0 M_S^2)} \approx 4 \text{ nm}$ while the characteristic length associated with the uniaxial anisotropy in regions A with a second-order uniaxial anisotropy $K_{2,A} = -1.5 \times 10^6 \text{ J/m}^3$ is $\lambda_A = \sqrt{A/|K_{2,A}|} \approx 3 \text{ nm}$ [19]. However, for a system comprised of regions A and B with different second-order uniaxial anisotropies one can expect the length scale $\lambda_{eff} = \sqrt{A/\left|\frac{\mu_0 M_S^2}{2} + \bar{K}_{2,eff}\right|} \approx 9 \text{ nm}$, associated with the sum of shape anisotropy and volume averaged anisotropy to play a more important role [19]. This length scale is shown as a gray vertical dashed line in Fig. 4.5 and can indeed be considered a characteristic length scale of the system.

D. Dynamic properties

To probe the dynamical response of the system a static magnetic field \vec{H} is applied either along the film normal ($\vec{H} = H \cdot \hat{z}$) or in the film plane ($\vec{H} = H \cdot \hat{y}$). Initially the system is relaxed in the presence of an additional small field \vec{h}_p perpendicular to the static magnetic field, i.e.

$\vec{H}_{total} = \vec{H} + \vec{h}_p$ (see Fig. 4.6). At $t = 0$ the small perpendicular field is removed and the time

evolution of the relaxation of the magnetization is recorded. The time evolution of the

magnetization in each cell of the micromagnetic model is described by the Landau-Lifshitz-

Gilbert equation of motion [20-23]:

$$\frac{d\vec{M}}{dt} = -\gamma \vec{M} \times \vec{H}_{eff} + \frac{1}{M_S} \vec{M} \times \alpha \frac{d\vec{M}}{dt} \quad (4.4)$$

where \vec{M} is the magnetization vector, M_S is the saturation magnetization, γ is the gyromagnetic

ratio and α is the damping parameter. The effective field \vec{H}_{eff} entering the Landau-Lifshitz-

Gilbert equation of motion includes the external magnetic field, dipole field, anisotropy field and

exchange field. In Fig. 4.7 (a) an example of the resulting time evolution of the average magnetization is shown when the external magnetic field is applied along the film normal. To enable a quantitative analysis of the time dependence of all cells in the simulation volume, we calculate the power spectral density for each cell and calculate the average power spectral density, as shown in Fig. 4.7 (b). The resulting spectrum reveals a number of resonant features that correspond to the fundamental resonance mode and higher order lateral standing spin wave modes in the structure. By plotting the contribution of each cell to the average power spectral density at the different resonant frequencies, one can visualize the mode profiles (see power spectral density maps shown as insets of Fig. 4.7 (b)).

For the fundamental mode in the out-of-plane configuration one notes that regions B with $K_{2,B} = 0 \text{ J/m}^3$ contribute significantly more to the power spectral density. In other words, the resonance is preferably localized in region B. In Fig. 4.8 the dependence of this localization on the lateral length scale of the anisotropy variations is quantified by plotting the ratio of the power spectral density contribution P_A of region A to the total power spectral density P_{total} . As expected in the limit of vanishing small length scales both regions contribute equally to the resonance, due to the strong exchange coupling between neighboring regions effectively averaging out the variations. As discussed above, when the static magnetic field is applied perpendicular to the film plane with increasing length scale of the lateral anisotropy variation the resonance becomes increasingly localized in region B, as expected [24]. However, in the in-plane case the situation is reversed, i.e. here with increasing length scale the resonance becomes increasingly localized in region A. In both cases the resonance is localized in the region of the structure with the lower excitation energy, as can be expected. Correspondingly this increased localization with increasing length scale of the lateral anisotropy variations causes the resonance frequency to

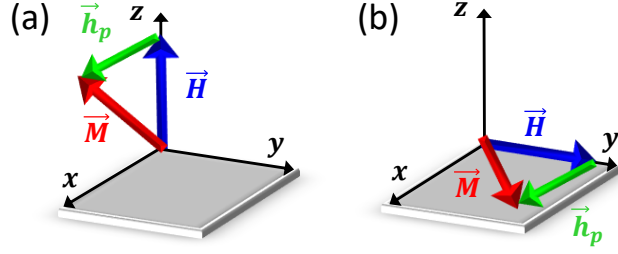


FIG. 4.6. Sketch of the configuration for determining the dynamic properties of the system. In (a) the out-of-plane configuration and in (b) the in-plane configuration is shown. The small additional field \vec{h}_p is only present during relaxation of the initial state and is removed at $t=0$.

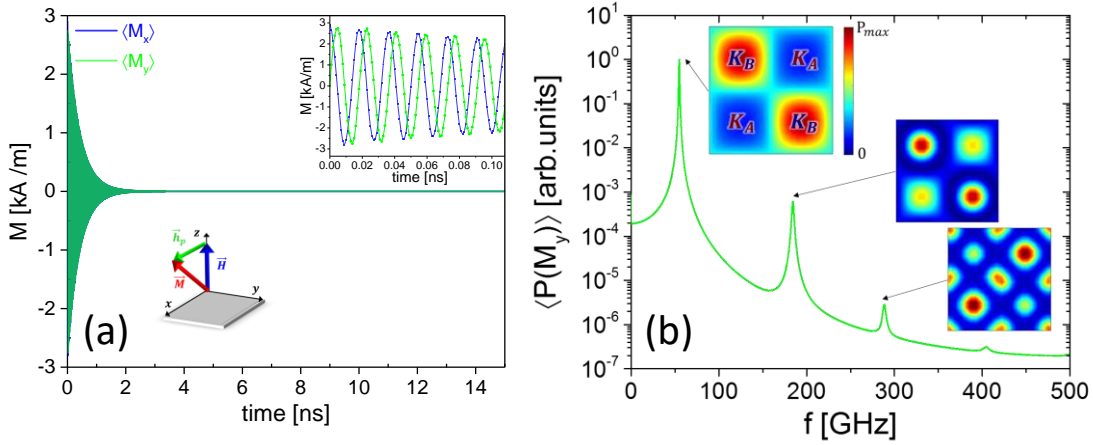


FIG. 4.7. (a) Time evolution of the average magnetization components $\langle M_x \rangle$ and $\langle M_y \rangle$ for a 20nm x 20nm structure with $K_{2,A} = -1.5 \times 10^{-6} \text{ J/m}^3$ and $K_B = 0 \text{ J/m}^3$ with an external magnetic field of $\mu_0 H = 2T$ applied along the film normal $\theta_H = 0^\circ$. The inset shows the time evolution during the first tenth of a nanosecond. (b) Shows $\langle P(M_y) \rangle$, i.e. the power spectral density of the y-component of the magnetization averaged over all cells in the simulation volume for the same parameters as in (a). The insets of this figure show the power spectral density maps for the first three resonances at frequencies $f_{\perp 1} = 54.9 \text{ GHz}$ (fundamental resonance mode), $f_{\perp 2} = 184 \text{ GHz}$ and $f_{\perp 3} = 288 \text{ GHz}$. Here the color indicates the contribution of each cell to the power spectral density, with dark red indicating the largest and dark blue zero contribution.

approach the resonance frequency f_B of a film with an anisotropy $K_{2,B}$ in the out-of-plane case, whereas in the same limit the resonance frequency in the in-plane case approaches the resonance frequency f_A of a film with an anisotropy $K_{2,A}$. This has important consequences for the effective anisotropies that one extracts from the dynamical data. The Kittel equations for systems with a second- and fourth-order perpendicular anisotropy are given by [16,25]:

$$f_{\perp} = \gamma'(H - M_{eff,\perp}) \quad (4.5-a)$$

$$f_{\parallel} = \gamma' \sqrt{H(H + M_{eff,\parallel})} \quad (4.5-b)$$

with $\gamma' = \gamma/2\pi$ and the effective out-of-plane and in-plane magnetizations given by:

$$M_{eff,\perp} = \frac{2\tilde{K}_{2,eff}^{dyn}}{\mu_0 M_S} + \frac{2K_{4,eff}^{dyn}}{\mu_0 M_S} \quad (4.6-a)$$

and

$$M_{eff,\parallel} = \frac{2\tilde{K}_{2,eff}^{dyn}}{\mu_0 M_S} \quad (4.6-b)$$

respectively.

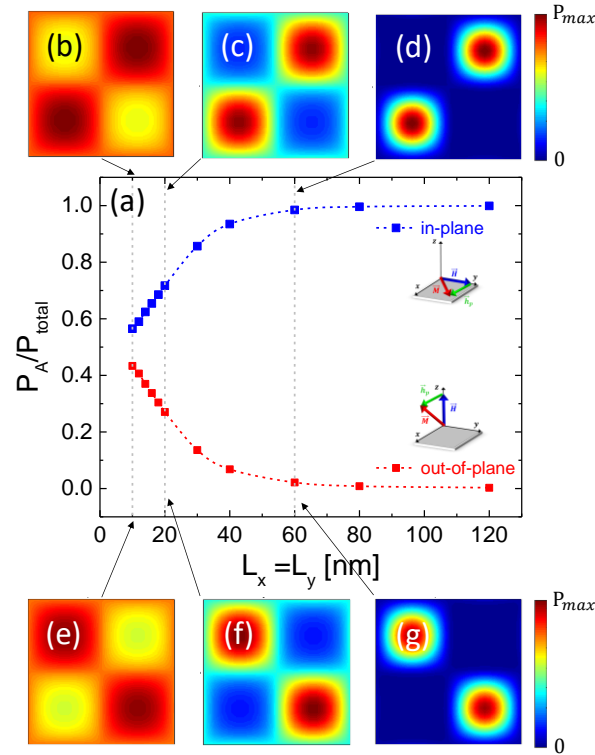


FIG. 4.8. (a) Dependence of the contribution of region A to the total power spectral density of the fundamental mode on the lateral length scale $L_{x,y}$ of the variations of the anisotropy. (b)-(d) show spectral maps with the static field applied in-plane whereas (e)-(g) show spectral maps with the static field applied out-of-plane. For (b) & (e) $L_x = L_y = 10$ nm, for (c) & (f) $L_x = L_y = 20$ nm and for (d) & (g) $L_x = L_y = 60$ nm.

From the numerical simulations one can therefore extract the dynamic effective second-order

uniaxial anisotropy $\tilde{K}_{2,eff}^{dyn}$ and effective fourth-order uniaxial anisotropy $K_{4,eff}^{dyn}$ that describe the

dynamical data in a macrospin approximation (see blue data points in Fig. 4.9). The definitions of $\tilde{K}_{2,eff}^{dyn}$ and $K_{4,eff}^{dyn}$ are the same as those of $\tilde{K}_{2,eff}$ and $K_{4,eff}$, the additional superscript indicating that these quantities are determined from the magnetization dynamics of the system. For comparison, the results from the quasi-static calculations (cp. Fig. 4.5 (a) and 4.5(b)) are also included in Fig. 4.9 (black data points). The limiting cases for the quantities determined from dynamical simulations can be understood as follows. For lateral anisotropy variations at vanishingly small length scales, i.e. $L_{x,y} \rightarrow 0$ the exchange coupling will effectively average out these variations and thus the effective second-order uniaxial anisotropy will approach the volume average of the two anisotropies $\bar{K}_{2,eff}$. In this limit the resonance has equal contributions from regions A and B for both the in-plane and out-of-plane configurations. Therefore, the effective magnetizations for both configurations will be equal and thus $K_{4,eff}^{dyn}$ vanishes for $L_{x,y} \rightarrow 0$ (see Fig. 4.9 (b)). For lateral anisotropy variations, over very large length scales, i.e. $L_{x,y} \rightarrow \infty$, the resonance in the out-of-plane configuration will become localized in region B whereas the resonance in the in-plane configuration will become localized in region A. Therefore

$$f_{\perp} \xrightarrow{L_{x,y} \rightarrow \infty} f_B \quad (4.7-a)$$

and

$$f_{\parallel} \xrightarrow{L_{x,y} \rightarrow \infty} f_A \quad (4.7-b)$$

and consequently:

$$\tilde{K}_{2,eff}^{dyn} \xrightarrow{L_{x,y} \rightarrow \infty} \frac{\mu_0 M_S^2}{2} + K_{2,A} \quad (4.8-a)$$

and

$$K_{4,eff}^{dyn} \xrightarrow{L_{x,y} \rightarrow \infty} K_{2,B} - K_{2,A} \quad (4.8-b)$$

As can be seen in Fig. 4.9 (a) and 4.9 (b) our simulation results for the dynamic higher order anisotropies approach these predicted values (blue dashed lines) for large length scales. However, the length scale dependence of the effective anisotropies obtained from the dynamic response of the system is significantly different from those obtained from quasi-static calculations for the same applied field. As these differences persist over the entire range of length scales of the anisotropy variations, including the asymptotic behavior at short and large length scales, we also expect a difference between the anisotropies obtained from quasi-static and dynamic measurements for physical samples. For those, interface roughness will lead to a continuous distribution of the second-order uniaxial anisotropy and the relevant length scales will be determined by the type of interface morphology present in the samples and its characteristic parameters [26].

The dynamic response of the system also shows a markedly different field dependence of the effective anisotropies when compared to the quasi-static results (see Fig. 4.4). While the effective anisotropies are weakly dependent on the external applied field through its influence on the equilibrium configuration of the magnetization the amount of localization has a much stronger influence. This is particularly evident for the dynamic fourth-order effective anisotropy which remains at a finite positive value even for the largest fields used in Fig. 4.4 (b), whereas the quasi-static results approach zero in this limit. We would like to point out that recent experimental observations of a field dependent of the second-order effective anisotropy [12] appear to be consistent with the predicted sensitivity of the effective anisotropies to the equilibrium configuration at low fields. Clearly more systematic experimental work is needed to verify whether spatial variations of the second-order anisotropy are indeed responsible for these observations.

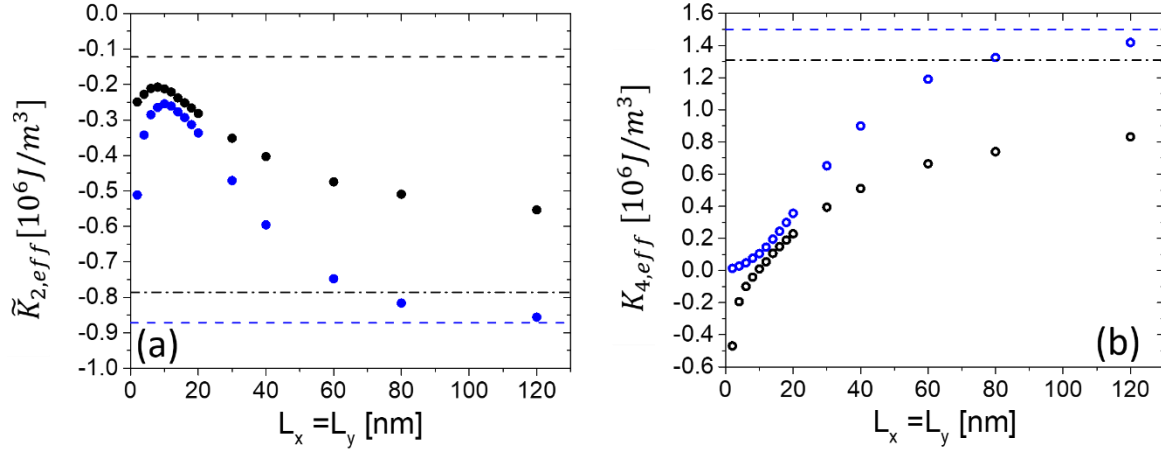


FIG. 4.9. Effective second-order uniaxial anisotropy as a function of the lateral length scale $L_{x,y}$ of the variations of the anisotropy. The anisotropy $\tilde{K}_{2,eff}^{dyn}$ for the dynamic simulations is shown as blue symbols whereas the anisotropy $\tilde{K}_{2,eff}$ determined from quasi-static simulations is shown as black symbols. The dashed black line shows the thin film limit with an average anisotropy, i.e. $\frac{\mu_0 M_S^2}{2} + \frac{K_{2,A} + K_{2,B}}{2}$. The dashed blue line represents the large length scale limit for the dynamical simulations $\frac{\mu_0 M_S^2}{2} + K_{2,A}$. (b) Effective fourth-order uniaxial anisotropy as a function of the lateral length scale $L_{x,y}$ of the variations of the anisotropy. The anisotropy $K_{4,eff}^{dyn}$ for the dynamic simulations is shown as blue symbols whereas the anisotropy $K_{4,eff}$ determined from quasi-static simulations is shown as black symbols. The dashed blue line represents the large length scale limit for the dynamical simulations $K_{2,B} - K_{2,A}$. In both figures the dash dotted black lines are the limiting values expected for the quasi-static effective anisotropies, obtained by treating each region as a macrospin and ignoring exchange interaction, see section C.

III. Summary and discussion

In summary, we have analyzed how lateral variations of a second-order uniaxial anisotropy affect the effective anisotropies required to describe the system in the framework of a macrospin model. For both quasi-static and dynamic calculations, we find that second-order and fourth-order effective anisotropies are sufficient to capture the properties of the system in the macrospin model. For the quasi-static properties, we find that the effective fourth-order uniaxial anisotropy is closely linked to deviations of the average magnetization angle from the field direction and the lateral variation of the magnetization direction in the structure. This results in a strong field dependence of the effective anisotropies. The dependence of the effective

anisotropies on the lateral length scale of the variations of the second-order uniaxial anisotropy are profoundly different for the quasi-static and dynamic calculations. The underlying reason for this difference is that the quasi-static properties are averaged over the entire sample volume whereas the observable dynamic properties depend sensitively on the degree of localization of the resonance. This localization depends not only on the lateral length scale of the anisotropy variations, but also on the field orientation. While there have also been some reports on the differences between anisotropies determined using quasi-static and dynamic methods [27-29], more experimental work is needed to clarify this aspect, particularly for systems with perpendicular anisotropy. Interpretation of experimental results for systems where lateral variations of the second-order anisotropy are caused by interfacial roughness will be complicated by the continuous distribution of anisotropies in the system. Thus, in order to make a quantitative comparison, a careful characterization of the interfacial roughness will be required [26,30]. However, we would like to point out that a continuous distribution of the second-order anisotropy is expected to result in a significant inhomogeneous broadening of the resonance that increases with the distribution of the anisotropy fields [24], very much in line with what has recently been reported for CoFe/Ni multilayers [31].

IV.Acknowledgments

This work was supported by NSF-CAREER Award No. 0952929 and by NSF-CAREER Award No. 1452670.

V. References

- [1] S. Mangin, Y. Henry, D. Ravelosona, J.A. Katine, and E.E. Fullerton, Reducing the critical current for spin-transfer switching of perpendicularly magnetized nanomagnets, *Applied Physics Letters* **94**, 012502 (2009), doi:<http://dx.doi.org/10.1063/1.3058680>.
- [2] E. Chen, D. Apalkov, A. Driskill-Smith, A. Khvalkovskiy, D. Lottis, K. Moon, V. Nikitin, A. Ong, X. Tang, S. Watts, R. Kawakami, M. Krounbi, S.A. Wolf, S.J. Poon, J.W. Lu, A.W. Ghosh, M. Stan, W. Butler, T. Mewes, S. Gupta, C.K.A. Mewes, P.B. Visscher, and R.A. Lukaszew, Progress and Prospects of Spin Transfer Torque Random Access Memory, *IEEE Transactions on Magnetics* **48**, 3025 (2012), 10.1109/TMAG.2012.2198451.
- [3] D. Weller, Y. Wu, J. Stöhr, M.G. Samant, B.D. Hermsmeier, and C. Chappert, Orbital magnetic moments of Co in multilayers with perpendicular magnetic anisotropy, *Physical Review B* **49**, 12888 (1994), <https://link.aps.org/doi/10.1103/PhysRevB.49.12888>.
- [4] J.M. Beaujour, D. Ravelosona, I. Tudosa, E.E. Fullerton, and A.D. Kent, Ferromagnetic resonance linewidth in ultrathin films with perpendicular magnetic anisotropy, *Physical Review B* **80**, 180415 (2009), <https://link.aps.org/doi/10.1103/PhysRevB.80.180415>.
- [5] J. Zhu, J.A. Katine, G.E. Rowlands, Y.-J. Chen, Z. Duan, J.G. Alzate, P. Upadhyaya, J. Langer, P.K. Amiri, K.L. Wang, and I.N. Krivorotov, Voltage-Induced Ferromagnetic Resonance in Magnetic Tunnel Junctions, *Physical Review Letters* **108**, 197203 (2012), <https://link.aps.org/doi/10.1103/PhysRevLett.108.197203>.
- [6] X. Ji, B. Liu, Y. Xu, H. Tang, X. Li, H. Gong, B. Shen, X. Yang, P. Han, and F. Yan, Deep-level traps induced dark currents in extended wavelength $\text{In}_x\text{Ga}_{1-x}\text{As}/\text{InP}$ photodetector, *Journal of Applied Physics* **114**, 224502 (2013), 10.1063/1.4838041.
- [7] K. Makoto, I. Hiroshi, T. Tomohiro, Y. Kay, K. Hitoshi, F. Akio, A. Koji, and Y. Shinji, Effect of MgO Cap Layer on Gilbert Damping of FeB Electrode Layer in MgO-Based Magnetic Tunnel Junctions, *Applied Physics Express* **6**, 073002 (2013), <http://stacks.iop.org/1882-0786/6/i=7/a=073002>.
- [8] P. Bruno, Tight-binding approach to the orbital magnetic moment and magnetocrystalline anisotropy of transition-metal monolayers, *Physical Review B* **39**, 865 (1989), <https://link.aps.org/doi/10.1103/PhysRevB.39.865>.
- [9] S. Ayaz Khan, P. Blaha, H. Ebert, J. Minár, and O. Šipr, Magnetocrystalline anisotropy of FePt: A detailed view, *Physical Review B* **94**, 144436 (2016), <https://link.aps.org/doi/10.1103/PhysRevB.94.144436>.

- [10] B. Heinrich, T. Monchesky, and R. Urban, Role of interfaces in higher order angular terms of magnetic anisotropies: ultrathin film structures, *Journal of Magnetism and Magnetic Materials* **236**, 339 (2001), [http://dx.doi.org/10.1016/S0304-8853\(01\)00455-3](http://dx.doi.org/10.1016/S0304-8853(01)00455-3).
- [11] F. Porrati, W. Wulfhekel, and J. Kirschner, An analytical model for ultrathin films with spatially varying magnetic anisotropies, *Journal of Magnetism and Magnetic Materials* **270**, 22 (2004), [http://dx.doi.org/10.1016/S0304-8853\(03\)00658-9](http://dx.doi.org/10.1016/S0304-8853(03)00658-9).
- [12] I. Barsukov, Y. Fu, A.M. Gonçalves, M. Spasova, M. Farle, L.C. Sampaio, R.E. Arias, and I.N. Krivorotov, Field-dependent perpendicular magnetic anisotropy in CoFeB thin films, *Applied Physics Letters* **105**, 152403 (2014), 10.1063/1.4897939.
- [13] <http://magneticslab.ua.edu/micromagnetics-code.html>.
- [14] A.J. Newell, W. Williams, and D.J. Dunlop, A generalization of the demagnetizing tensor for nonuniform magnetization, *Journal of Geophysical Research: Solid Earth* **98**, 9551 (1993), 10.1029/93JB00694.
- [15] IFC (Ed. Board), *Physica B: Condensed Matter* **343**, IFC (2004), [https://doi.org/10.1016/S0921-4526\(03\)01103-7](https://doi.org/10.1016/S0921-4526(03)01103-7).
- [16] J.M. Shaw, H.T. Nembach, M. Weiler, T.J. Silva, M. Schoen, J.Z. Sun, and D.C. Worledge, Perpendicular Magnetic Anisotropy and Easy Cone State in Ta/Co₆₀Fe₂₀B₂₀/MgO, *IEEE Magnetics Letters* **6**, 1 (2015), 10.1109/LMAG.2015.2438773.
- [17] K.A. Seu, S. Roy, J.J. Turner, S. Park, C.M. Falco, and S.D. Kevan, Cone phase and magnetization fluctuations in Au/Co/Au thin films near the spin-reorientation transition, *Physical Review B* **82**, 012404 (2010), <https://link.aps.org/doi/10.1103/PhysRevB.82.012404>.
- [18] R.L. Stamps, L. Louail, M. Hehn, M. Gester, and K. Ounadjela, Anisotropies, cone states, and stripe domains in Co/Pt multilayers, *Journal of Applied Physics* **81**, 4751 (1997), 10.1063/1.365452.
- [19] A.H.a.R. Schäfer, *Magnetic Domains* (Springer-Verlag, Berlin Heidelberg 1998).
- [20] T.L. Gilbert, *Physical Review* **100**, 1243 (1955), [Abstract only, not online; full report, Armor Research Foundation Project No. A059, Supplementary Report, May 1, 1956] (unpublished).
- [21] T.L. Gilbert, A phenomenological theory of damping in ferromagnetic materials, *IEEE Transactions on Magnetics* **40**, 3443 (2004), 10.1109/TMAG.2004.836740.
- [22] A. Aharoni, *Introduction to the Theory of Ferromagnetism* (Oxford University Press 2001).

- [23] C.K.A. Mewes and T. Mewes, in *Handbook of Nanomagnetism* (Pan Stanford, 2015), pp. 71.
- [24] R.D. McMichael, D.J. Twisselmann, and A. Kunz, Localized Ferromagnetic Resonance in Inhomogeneous Thin Films, *Physical Review Letters* **90**, 227601 (2003), <https://link.aps.org/doi/10.1103/PhysRevLett.90.227601>.
- [25] Z.R. Tadisina, A. Natarajarathinam, B.D. Clark, A.L. Highsmith, T. Mewes, S. Gupta, E. Chen, and S. Wang, Perpendicular magnetic tunnel junctions using Co-based multilayers, *Journal of Applied Physics* **107**, 09C703 (2010), doi:<http://dx.doi.org/10.1063/1.3358242>.
- [26] Y.P. Zhao, G. Palasantzas, G.C. Wang, and J.T.M. De Hosson, Surface/interface-roughness-induced demagnetizing effect in thin magnetic films, *Physical Review B* **60**, 1216 (1999), <https://link.aps.org/doi/10.1103/PhysRevB.60.1216>.
- [27] R. Lopusnik, J.P. Nibarger, T.J. Silva, and Z. Celinski, Different dynamic and static magnetic anisotropy in thin Permalloy™ films, *Applied Physics Letters* **83**, 96 (2003), 10.1063/1.1587255.
- [28] M.L. Schneider, A.B. Kos, and T.J. Silva, Dynamic anisotropy of thin Permalloy films measured by use of angle-resolved pulsed inductive microwave magnetometry, *Applied Physics Letters* **86**, 202503 (2005), 10.1063/1.1923193.
- [29] D. Xue and X. Fan, Comment on “Dynamic anisotropy of thin Permalloy films measured by use of angle-resolved pulsed inductive microwave magnetometry” [*Appl. Phys. Lett.* 86, 202503 (2005)], *Applied Physics Letters* **90**, 116101 (2007), 10.1063/1.2713125.
- [30] T. Mewes, M. Rickart, A. Mougin, S.O. Demokritov, J. Fassbender, B. Hillebrands, and M. Scheib, Comparative study of the epitaxial growth of Cu on MgO(001) and on hydrogen terminated Si(001), *Surface Science* **481**, 87 (2001), [http://dx.doi.org/10.1016/S0039-6028\(01\)01000-7](http://dx.doi.org/10.1016/S0039-6028(01)01000-7).
- [31] J.M. Shaw, H.T. Nembach, and T.J. Silva, Resolving the controversy of a possible relationship between perpendicular magnetic anisotropy and the magnetic damping parameter, *Applied Physics Letters* **105**, 062406 (2014), 10.1063/1.4892532.

5. CONCLUSION

In this dissertation, magnetic anisotropies and magnetization dynamics in multilayered thin films have been investigated. In the second chapter, magnetization dynamics in a system with exchange bias effect, and a uniaxial Perpendicular Magnetic Anisotropy (PMA) are discussed. Broadband ferromagnetic resonance results are analyzed to study the unidirectional anisotropy in these films. In addition, a unidirectional relaxation mechanism is observed in a CoFe/IrMn bilayer. To understand the origin of the unidirectional relaxation, a thickness series is analyzed using an experimental approach and numerical analysis. Our results confirm that the unidirectional mechanism includes two contributions: (1) an inverse thickness-squared contribution, and (2) a second term that scales with the inverse thickness. The inverse thickness-squared dependence of the Gilbert damping parameter in these multilayers indicates that the two-magnon scattering contributes to the relaxation. The contribution that scales with the inverse thickness on the other hand has not been previously identified and more theoretical and experimental work will be required to obtain a better understanding of this origin. In addition, it has been shown that the interface energy of the exchange bias effect exceeds the values that are previously reported for metallic antiferromagnetic materials in exchange biased systems. Moreover, we observed a significant misalignment between the magnetization and the applied magnetic field for specific applied field orientations. Our numerical analysis suggests that if one does not consider this misalignment, this will result in a non-physical threefold symmetry in the

residuals of the fit to the angular dependence of the resonance field. As a future project, this misalignment can be observed with methods such as the X-Ray Magnetic Circular Dichroism (XMCD) and the Polarized Neutron Reflectivity (PNR) experiments. In addition, one can look at bilayers where the unidirectional anisotropy is perpendicular to the film instead of being in the plane of the film. This becomes very important because most proposed spintronic devices depend on a strong perpendicular magnetic anisotropy.

In chapter three, we have presented the magnetization dynamic analyses in $\text{SiO}_2/\text{Ni}_{0.8}\text{Fe}_{0.2}/\text{SiO}_2$, $\text{SiO}_2/\text{Ni}_{0.8}\text{Fe}_{0.2}/\text{Ru}$, and $\text{Ru}/\text{Ni}_{0.8}\text{Fe}_{0.2}/\text{Ru}$ multilayers. Using broadband FMR, we have investigated the thickness dependence of the effective magnetization and the Gilbert damping parameter in these multilayers. The thickness dependence of the effective magnetization confirms the presence of PMA that originates from both the SiO_2 - $\text{Ni}_{0.8}\text{Fe}_{0.2}$ and the Ru - $\text{Ni}_{0.8}\text{Fe}_{0.2}$ interfaces. Our results confirm the presence of a strong PMA in SiO_2 - $\text{Ni}_{0.8}\text{Fe}_{0.2}$ interfaces.

For a fundamental understanding of the interfacial PMA in these systems, we have initiated theoretical research to study the interfacial PMA at the $\text{Ni}_{0.75}\text{Fe}_{0.25}$ -normal metal interface. This normal metal can be Cu, Ta, Ru, Pt, etc. The initial results are very promising and call for extensive research in this field for fundamental and commercial interest. More work needs to be done to search for materials with a strong interfacial PMA.

In chapter four, we have performed micromagnetic simulations to model the spatial fluctuations in systems with uniaxial PMA. We have investigated the angular dependence of the magnetic energy and the magnetization dynamics in such systems. Our studies confirm the presence of a fourth-order uniaxial PMA, with an opposite sign than the sign of the second-order uniaxial PMA, that is a result of the lateral inhomogeneity in the second-order uniaxial PMA. In

addition, the effect of the length scale of the fluctuations on the magnetic energy and the dynamical response of the system is discussed in detail in chapter four.

Quasi-static higher-order anisotropy is related to the misalignment of the magnetization and the applied magnetic field and shows a field dependence. In addition, quasi-static higher-order anisotropy has a strong dependence on the length scale of the inhomogeneities comparing to the higher order anisotropy that is obtained from the dynamical response. We conclude that in the quasi-static method, the resulting properties are averaged over the structure while the dynamical response of the system reflects the local resonances that are present in the system.

6. REFERENCES

- [1] T.L. Gilbert, A Lagrangian formulation of the gyromagnetic equation of the magnetic field, *Phys. Rev.* 100 (1955).
- [2] T.L. Gilbert, A phenomenological theory of damping in ferromagnetic materials, *IEEE Transactions on Magnetics* 40, 3443 (2004), [10.1109/TMAG.2004.836740](http://dx.doi.org/10.1109/TMAG.2004.836740).
- [3] J.C. Slonczewski, Current-driven excitation of magnetic multilayers, *Journal of Magnetism and Magnetic Materials* 159, L1 (1996), [http://dx.doi.org/10.1016/0304-8853\(96\)00062-5](http://dx.doi.org/10.1016/0304-8853(96)00062-5).
- [4] E.L. L. Landau, On The Theory Of the Dispersion of Magnetic Permeability in Ferromagnetic Bodies *Phys. Z. Sowjetunion* 8, 153 (1935).
- [5] A.G. Gurevich and G.A. Melkov, *Magnetization Oscillation and Waves* (CRC. Press Inc. , Boca Raton, Florida, 1996), Vol. 1.
- [6] W.F. Brown, *Magnetostatic Principles in Ferromagnetism* (North Holland Publishing Co., Amsterdam, 1962).
- [7] A. Aharoni, *Introduction to the Theory of Ferromagnetism* (Oxford University Press, New York, 2000), Second edn.
- [8] W.H. Meiklejohn and C.P. Bean, New Magnetic Anisotropy, *Physical Review* 102, 1413 (1956), <https://link.aps.org/doi/10.1103/PhysRev.102.1413>.
- [9] J. Nogués and I.K. Schuller, Exchange bias, *Journal of Magnetism and Magnetic Materials* 192, 203 (1999), [http://dx.doi.org/10.1016/S0304-8853\(98\)00266-2](http://dx.doi.org/10.1016/S0304-8853(98)00266-2).
- [10] J. Smit and H.G. Beljers, Ferromagnetic Resonance Absorption in BaFe₁₂O₁₉, A Highly Anisotropic Crystal, *Philips Res. Rep* 10, 28 (1955).
- [11] J. Jorzick, S.O. Demokritov, C. Mathieu, B. Hillebrands, B. Bartenlian, C. Chappert, F. Rousseaux, and A.N. Slavin, Brillouin light scattering from quantized spin waves in micron-size magnetic wires, *Physical Review B* 60, 15194 (1999), <https://link.aps.org/doi/10.1103/PhysRevB.60.15194>.
- [12] M. Farle, Ferromagnetic resonance of ultrathin metallic layers, *Reports on Progress in Physics* 61, 755 (1998), <http://stacks.iop.org/0034-4885/61/i=7/a=001>.

- [13] C.J. Oates, F.Y. Ogrin, S.L. Lee, P.C. Riedi, G.M. Smith, and T. Thomson, High field ferromagnetic resonance measurements of the anisotropy field of longitudinal recording thin-film media, *Journal of Applied Physics* 91, 1417 (2002), 10.1063/1.1428804.
- [14] C.P. Poole, *Electron Spin Resonance A Comprehensive treatise on Experimental Techniques* (Dover ed., Mineola, N. Y. , 1983).
- [15] J.M. Shaw, H.T. Nembach, T.J. Silva, and C.T. Boone, Precise determination of the spectroscopic g-factor by use of broadband ferromagnetic resonance spectroscopy, *Journal of Applied Physics* 114, 243906 (2013), 10.1063/1.4852415.
- [16] B. Heinrich, J.F. Cochran, and R. Hasegawa, FMR linebroadening in metals due to two-magnon scattering, *Journal of Applied Physics* 57, 3690 (1985), 10.1063/1.334991.
- [17] S.S. Kalarickal, P. Krivosik, M. Wu, C.E. Patton, M.L. Schneider, P. Kabos, T.J. Silva, and J.P. Nibarger, Ferromagnetic resonance linewidth in metallic thin films: Comparison of measurement methods, *Journal of Applied Physics* 99, 093909 (2006), 10.1063/1.2197087.
- [18] B. Voigtländer, in *Scanning Probe Microscopy: Atomic Force Microscopy and Scanning Tunneling Microscopy* (Springer Berlin Heidelberg, Berlin, Heidelberg, 2015), pp. 101.
- [19] C.V. Thompson and R. Carel, Texture development in polycrystalline thin films, *Materials Science and Engineering: B* 32, 211 (1995), [http://dx.doi.org/10.1016/0921-5107\(95\)03011-5](http://dx.doi.org/10.1016/0921-5107(95)03011-5).
- [20] M.K. Puchert, P.Y. Timbrell, and R.N. Lamb, Postdeposition annealing of radio frequency magnetron sputtered ZnO films, *Journal of Vacuum Science & Technology A: Vacuum, Surfaces, and Films* 14, 2220 (1996), 10.1116/1.580050.
- [21] J. Serafinczuk, J. Pietrucha, G. Schroeder, and T.P. Gotszalk, Thin film thickness determination using X-ray reflectivity and Savitzky–Golay algorithm *Optica Applicata XLI* (2011).
- [22] M3 Micromagnetics Code, <http://magneticslab.ua.edu/micromagnetics-code.html>.
- [23] J. Lenz and S. Edelstein, Magnetic sensors and their applications, *IEEE Sensors Journal* 6, 631 (2006), 10.1109/JSEN.2006.874493.
- [24] U. Gradmann, Ferromagnetism near surfaces and in thin films, *Applied physics* 3, 161 (1974), 10.1007/bf00884493.
- [25] B.N. Engel, C.D. England, R.A. Van Leeuwen, M.H. Wiedmann, and C.M. Falco, Interface magnetic anisotropy in epitaxial superlattices, *Physical Review Letters* 67, 1910 (1991), <https://link.aps.org/doi/10.1103/PhysRevLett.67.1910>.

- [26] J. Beik Mohammadi, J.M. Jones, S. Paul, B. Khodadadi, C.K.A. Mewes, T. Mewes, and C. Kaiser, Broadband ferromagnetic resonance characterization of anisotropies and relaxation in exchange-biased IrMn/CoFe bilayers, *Physical Review B* 95, 064414 (2017), <https://link.aps.org/doi/10.1103/PhysRevB.95.064414>.
- [27] C.K. Mewes and T. Mewes, *Relaxation in magnetic materials for spintronics* (Pan Stanford Publishing Singapore, 2015).
- [28] T. Mewes, R.L. Stamps, H. Lee, E. Edwards, M. Bradford, C.K.A. Mewes, Z. Tadisina, and S. Gupta, Unidirectional Magnetization Relaxation in Exchange-Biased Films, *IEEE Magnetism Letters* 1, 3500204 (2010), 10.1109/LMAG.2010.2055552.
- [29] K. Lee, J.J. Sapan, S.H. Kang, and E.E. Fullerton, Perpendicular magnetization of CoFeB on single-crystal MgO, *Journal of Applied Physics* 109, 123910 (2011), 10.1063/1.3592986.
- [30] J. Beik Mohammadi, C. Mewes, T. Mewes, and G. Mankey, Ferromagnetic resonance study of interfacial perpendicular anisotropy in Ni_{0.8}Fe_{0.2}/Ru and Ni_{0.8}Fe_{0.2}/SiO₂ interfaces, *Applied Physics Letters* (in preparation).
- [31] J. Beik Mohammadi, K. Cole, C. Mewes, and T. Mewes, Micromagnetic Investigations of Higher Order Anisotropy in Ultra-thin Films with Fluctuating Perpendicular Anisotropy, (submitted to *Physical Review B*).